



**University of
Zurich^{UZH}**

UNIVERSITY OF ZURICH
INSTITUTE OF COMPUTATIONAL SCIENCE

A sub-grid model for molecular gas in a cosmological galaxy formation simulation

Author:

Amandeep Singh

Supervisor:

Prof. (Dr.) Romain
Teyssier

A thesis submitted for the degree of
MSc Physics - Theoretical Astrophysics and Cosmology

July 18, 2019

Acknowledgements

First and foremost, I would like to express my wholehearted gratitude to my Supervisor, Prof. (Dr.) Romain Teyssier for his unflinching faith in my potential, unique way of guidance, moral and technical support. It was sheer because of his micro-planning, meticulous approach and untiring and thorough efforts that kept me self-motivated all through this wonderful journey. From the time I have been associated with him in connection with my Thesis, I realised that he is not only knowledgeable, patient, diligent and persistent gentleman, but also a dynamic and humble, but firm, human being with all ingredients of a balanced Supervisor. His zeal and exuberance also encouraged me to draw inspiration. He gave me full liberty to experiment on my own while being watchful himself. I certainly owe a lot to Prof. (Dr.) Romain Teyssier for nurturing and enlightening me with his vast experience and reservoir of wisdom.

I would avail of this opportunity to graciously thank Mr. Michael Kretschmer and Ms. Tine Colman, for their valuable and constructive suggestions during the planning and development of this project as well as their assistance in keeping my progress on schedule. On my part, I also wish them good luck for their future endeavours.

I would also like to extend my sincere appreciation to the Institute of Computational Science and all its members for their ceaseless assistance in offering me the required resources and helped me, in one way or the other, in timely completion of my Thesis.

Finally, I wish to thank my parents and sister for their support - moral as well as financial as also for inculcating good human and religious values in me.

Last but not the least, I would like to undertake that I shall continue to progress conscientiously and assiduously and feel all those proud, who have been associated with me during this remarkable journey.

Amandeep Singh

July 18, 2019

Abstract

A model is constructed that uses Jeans length and virial theorem to establish a relation between the radius and density of a macroscopic volume element. The molecular fractions of H_2 and CO are computed, also taking into account the self-shielding effect of H_2 . Then, a simplified model for radiative transfer is introduced to compute the emissivity and line emission of CO . This sub-grid model is then used to post process a cosmological zoom-in simulation of a $z \approx 0.6$ galaxy ($M_\star \approx 10^{10}M_\odot$, $SFR \approx 2M_\odot\text{yr}^{-1}$) to study the spectral energy distribution, line luminosity, and molecular fraction of CO. The total luminosity of the galaxy computed for $CO(1 - 0)$ transition using velocity dispersion Δv is $L_{CO} = 19.48 \times 10^8 \text{Kkm s}^{-1} \text{pc}^2$, while total luminosity of the galaxy using isothermal sound speed $c_{s,CO}$ is $L_{CO} = 0.73 \times 10^8 \text{Kkm s}^{-1} \text{pc}^2$. The total mass of H_2 in the galaxy is computed to be $M_{H_2} = 2.863 \times 10^9 M_\odot$. Using velocity dispersion Δv , $\alpha_{CO,TOT}^{-1} = 0.684 \text{Kkm s}^{-1} \text{pc}^2 M_\odot^{-1}$, while using isothermal sound speed $c_{s,CO}$, $\alpha_{CO,TOT}^{-1} = 0.0258 \text{Kkm s}^{-1} \text{pc}^2 M_\odot^{-1}$.

Contents

List of Figures	6
List of Tables	7
1 Introduction	8
1.1 The space between stars	8
1.2 Characteristics of the ISM	9
1.3 Giant Molecular Clouds (GMCs)	9
1.4 Line Transfer	11
1.4.1 Energy levels and their occupation numbers	11
1.4.2 Partition function	12
1.4.3 Line Emission and Absorption - Einstein Coefficients	13
1.4.4 Line profile function ($\phi_{ij}(\nu)$)	14
1.4.5 Photon escape probability and optical depth	15
2 Model Outline	17
2.1 Some definitions	17
2.1.1 Different scales in the model	17
2.1.2 Turbulence	17
2.1.3 Sonic Length	17
2.2 Density field of the sub-grid model	18
2.3 Length scale of the absorbing layer	18
2.4 Power-law PDF due to self-gravity	19
2.5 H_2 formation model	20
2.6 Self Shielding of H_2	21
2.7 CO formation model	22
2.8 Line radiative transfer	23
3 Results from the Sub-Grid Model	25
3.1 Log-normal PDF vs Power-law PDF	25
3.2 Length scale of the absorbing layer	25
3.3 Molecular fractions of H_2 and CO	25
3.4 Line optical depth and luminosity density	27
4 Application of the model on a Simulation	30
4.1 Salient features	30
4.2 Model Predictions	32
4.3 Applying the sub-grid model on the simulation	35

5 Conclusion	41
6 Further Work	44
References	45

List of Figures

1	$\log(n_H)$ vs PDF and $\log(\text{PDF})$: Comparing the log-normal PDF and the power-law PDF. The mach number here is $\mathcal{M} = 10$.	26
2	$\log n_H$ vs $\log \text{PDF}$: Varying \mathcal{M} for the log-normal PDF. As the Mach number is increased, the PDF expands, i.e., the mass increases. The opposite effect is observed when the Mach number is decreased.	27
3	$\log(n_H)$ vs $\log(\lambda_J)$: Plotting the length of the absorbing layer as function of the density of the cloud.	27
4	The number of photo-dissociating LW photons and the molecular fraction of H_2 plotted as function of the density of the cloud - with and without self shielding.	28
5	$\log(n_H)$ vs X_{CO} : Molecular fraction of CO plotted as function of the density of the cloud (self-shielding effects for CO not included).	28
6	The optical depth and the escape probability for the emitted photons is plotted as a function of the density of the cloud - using isothermal sound speed, and using different values of velocity dispersion Δv .	29
7	$\log(n_H)$ vs $\log(\alpha_{CO}^{-1})$: the sub-grid α_{CO}^{-1} factor of line emission of CO plotted as function of the density of the cloud - using isothermal sound speed, and using different values of velocity dispersion Δv .	30
8	$\overline{X_{H_2}}$ vs $\overline{n_H}$: Varying \mathcal{M} - Model prediction.	33
9	$\overline{X_{CO}}$ vs $\overline{n_H}$: Varying \mathcal{M} - Model prediction.	33
10	$\overline{X_{H_2}}$ vs $\overline{n_H}$: Varying Z - Model prediction.	34
11	$\overline{X_{CO}}$ vs $\overline{n_H}$: Varying Z - Model prediction.	34
12	$\overline{X_{H_2}}$ vs $\overline{n_H}$: Varying G_0 - Model prediction.	35
13	$\overline{X_{CO}}$ vs $\overline{n_H}$: Varying G_0 - Model prediction.	36
14	$\log(\alpha_{CO}^{-1})$ vs $\overline{n_H}$: for $c_{s,CO}$ and Δv - Model prediction.	36
15	$\overline{X_{H_2}}$ vs $\overline{n_H}$: Plotting the variation of \mathcal{M} - Applying sub-grid model on the simulation.	37
16	$\overline{X_{CO}}$ vs $\overline{n_H}$: Plotting the variation of \mathcal{M} - Applying sub-grid model on the simulation.	38
17	$\overline{X_{H_2}}$ vs $\overline{n_H}$: Plotting the variation of Z - Applying sub-grid model on the simulation.	39

18	$\overline{X_{CO}}$ vs $\overline{n_H}$: Plotting the variation of Z - Applying sub-grid model on the simulation.	40
19	$\log(\alpha_{CO}^{-1})$ vs $\log(\overline{n_H})$: Using the Δv and $c_{s,CO}$ values from the simulation - Applying sub-grid model on the simulation.	40
20	$\overline{X_{H_2}}$ vs $\overline{n_H}$: Galaxy map of the molecular fraction of H_2 - Applying sub-grid model on the simulation.	41
21	$\overline{X_{CO}}$ vs $\overline{n_H}$: Galaxy map of the molecular fraction of CO - Applying sub-grid model on the simulation.	42
22	α_{CO}^{-1} vs $\overline{n_H}$: Galaxy map of the α_{CO}^{-1} factor for line emission of CO - Applying sub-grid model on the simulation.	43

List of Tables

1	Some well known numerical values for our Galaxy[1].	8
2	Summary of the properties of clouds and other regions found in the interstellar medium [1]	10

1 Introduction

1.1 The space between stars

Till mid-1960's, the region between the stars (interstellar space) was considered to be too hostile for the existence of appreciable quantities of molecules. This assumption started to be questioned in early- 1970's when fragile molecule such as NH_3 , H_2O and H_2CO were observed. These observations led to the onset of rigorous studies and modelling of chemistry in the interstellar medium (ISM).

The conditions in the ISM are studied by observing the radiation absorbed and emitted by atoms and molecules. The atomisation of these observations leads to the modelling of the physics in the clouds of interstellar matter that fill our Galaxy. This modelling helps us to predict the presence of unobservable or unobserved phenomenon, which extends our knowledge of the behaviour of atoms and molecules under a unique set of physical conditions.

In our Galaxy, the distribution of matter in – between stars is far from uniform. From observations of our own Galaxy and of other galaxies, it is known that matter tends to be concentrated in filaments approximating the arms of a spiral. Values of some relevant physical properties of our galaxy are summarised in Table 1[1]. Young stars are concentrated within these spiral arms and form out the clouds of gas and dust that are present in these regions.

the Milky Way: numerical values	
Age of Galaxy	1.2×10^{10} yr
Diameter	25 kpc
Thickness	250 pc
Mass	$1.4 \times 10^{10} M_\odot$
Overall density	$7 \times 10^{-24} g\ cm^{-3}$
1 Parsec (pc) = $3.086 \times 10^{18} cm$	
Mass of Sun(M_\odot) = $1.986 \times 10^{33} g$	

Table 1: Some well known numerical values for our Galaxy[1].

1.2 Characteristics of the ISM

The space between stars is filled with gas and dust, this is known as the Interstellar medium (ISM). Generally, ISM has low densities and low temperatures, but extreme regions with large variations in density and temperature also exist. The ISM reaches to the atmosphere of stars. Hydrogen in the region of ISM around a young star is ionised by ultraviolet radiation from the star. This created a spherical region of ionised gas, called HII region, that is transparent to radiation with $E > 13.6\text{eV}$.

The process of star formation in a Giant molecular cloud leads to the formation of local regions where the gas is highly excited in the visible, infrared and microwave regions of the spectrum. Diffuse clouds of interstellar matter are transparent to UV ad visible radiation. The spectral features shown by these clouds are due to the presence of various simpler molecules and the emission lines of atoms and ions. In these clouds, most of the H is converted into H_2 . This process is aided by the process of self-absorption in photo dissociating transitions in H_2 which creates shielding effect [2] [3] [4].

A summary of the properties of clouds and other region in the ISM can be found in Table 2[1].

1.3 Giant Molecular Clouds (GMCs)

The interstellar space is filled with ultraviolet radiation from stars. This background radiation is responsible for breaking apart molecules into atoms, a process known as photo-dissociation. These photons are usually in the Lyman-Werner (LW) energy band: $11 - 13.6\text{eV}$. Detailed discussion in sections 2.5 and 2.6.

Interstellar space also contains significant amounts of dust capable of blocking out starlight. When this dust accumulates, it forms a region in which the ultraviolet radiation from stars is blocked. This allows for the formation of molecules such as H_2 , CO , H_2O , NH_3 , CH , CN , etc. [5]. As these molecules begin to accumulate, gravity pulls all the gas together to form large gas structures known as Giant Molecular clouds (GMCs). The average density within these clouds is $10^2 - 10^3 \text{H/cc}$, which is much denser than the surrounding interstellar space [1]. As a result, though they account for a very small fraction of the volume of interstellar space, they contain a significant fraction- 20% – 30% - of the Milky Way's gas. [6]

Because of their high density, molecular clouds block UV starlight, which is responsible for heating most interstellar gas. As a result, the typical tem-

Object	Properties*
HII region	$T \approx 10000\text{K}$, Dominant ion H^+ , $n \approx 10^2 - 10^3\text{cm}^{-3}$.
Diffuse Clouds	$T \approx 100\text{K}$, Partial conversion of H into H_2 , Other atoms partially neutral, $n \approx 100\text{cm}^{-3}$, Molecules CO , H_2CO , and some others observed.
Clumps/Clouds/Fragments	$T = 10 - 20\text{K}$, Most H converted into H_2 , Large optical depth in visible and ultraviolet, $n \approx 10^4\text{cm}^{-3}$, Little internal motion, $M = 10^2 - 10^4M_\odot$, $r \approx 5\text{ pc}$, Many molecules observed.
Giant Molecular Clouds	$T \approx 10\text{K}$, Relatively low density $n \approx 600\text{cm}^{-3}$, Very large mass $M \approx 10^5M_\odot$, Diameter $40 - 100\text{ pc}$.

* T = kinetic temperature, n = number of H -atoms cm^{-3} in all forms,
 M = Mass, r = radius.

Table 2: Summary of the properties of clouds and other regions found in the interstellar medium [1]

perature of molecular gas clouds is $\approx 10\text{K}$ [1] [6]. These clouds are massive, with sizes up to 100pc across and masses often ranging from $1 - 2 \times 10^5$ solar masses [1].

It is estimated that 3000–4000 clouds exist in our galaxy [1]. The density within these clouds is not uniform. The region with higher density, where lots of dust and gas cores reside, are called *clumps*. If the gravity in these clumps is able to overcome the high density, and forces the dust and gas to collapse, then these clumps will begin to form stars [6]. The process of formation of these clumps in the cloud is called fragmentation.

A good way to study the characteristics of a GMC would be to observe the emission and absorption spectra of its constituent atoms and molecules.

The most abundant molecule in these clouds is molecular hydrogen (H_2). But H_2 lacks an electric dipole so its first quadruple line excitation temperature ($T_{exc} \approx 500\text{K}$) is much higher than the kinetic temperature of the surrounding molecular cloud ($T_K \approx 10\text{K}$) [1] [7]. This means that it is not possible to observe H_2 directly since it does not radiate or absorb even at radio wavelengths. Carbon monoxide (CO), which is the second most abundant molecule in these clouds, conveniently also has a low excitation temperature ($T_{exc} \approx 5\text{K}$) [1] [7]. This means that CO is easily excited inside the molecular cloud. Our knowledge of these clouds and their internal state comes from the observations of radio lines from ^{12}CO and ^{13}CO . Since CO tends to be present wherever H_2 is found [1] [6], the frequencies emitted from CO molecules and the strength of the corresponding spectral lines enable astronomers to infer the H_2 density in the emitting region.

1.4 Line Transfer

Molecular clouds consist of dust and gas. The gas in the clouds can be studied by observing the emission and absorption spectra of the gas molecules. The gas atoms or molecules have discrete energy states. These spectral lines can be observed when the atom or molecule jumps from one energy state to another. These are called *bound-bound transitions* and are ruled by quantum mechanics. If such transitions occur due to collisions between atoms or molecules, they are called *collisional transitions*. And if such transitions occur by emitting or absorbing a photon, they are *radiative transitions*. Radiative transitions are the main ingredient in line radiative transfer. [8]

1.4.1 Energy levels and their occupation numbers

Let the total number of energy states/levels of an atom or molecule be N_{levels} . If, $i = 1, 2, \dots N_{levels}$, then energy of each level is denoted as E_i , and in ascending order of energies the order is : $E_{i+1} \geq E_i$.

Now, if n is the total number density of atoms or molecules per cubic cm, and n_i gives the occupation number density belonging to each level, then, $n = \sum_i n_i$.

The *fractional occupation number* x_i is then defined as:

$$x_i = \frac{n_i}{n}, \quad (1)$$

such that $\sum_i x_i = 1$. One of the tasks of line radiative transfer is to compute n_i .

Collisions between atoms or molecules can cause the atom/molecule to transit from any state i to other state j . When density is high, these collisions take place so often that it can be assumed that x_i are thermally distributed, i.e.,

$$\frac{x_j}{x_i} = \frac{n_j}{n_i} = \frac{g_j}{g_i} e^{-(E_j - E_i)/k_B T} \quad (2)$$

where:

- k_B = Boltzmann's constant,
- T = Temperature of the gas,
- g_i, g_j = Statistical weights of the corresponding energy levels.

If this can be assumed at some location, the system is said to be in local thermodynamic equilibrium (LTE).

If the density is very, the radiative transitions may become more frequent than collisional transitions, and this would lead to a non-LTE system in which the level populations cannot be computed using equation 2. Equation 2 is known as the Boltzmann equation for LTE.

For Non-LTE, equation 2 is not valid. In non-LTE, the temperature is not constant at 10K, it varies between the background temperature ($T_{CMB} = 2.73\text{K}$) and the mean temperature ($\bar{T} = 10\text{K}$). To include this variation of temperature, full scale radiative transfer models have to included. It was observed in this model that the results obtained by assuming LTE were accurate enough for H_2 and CO . So, LTE regime is considered in this model hereafter. The non-LTE regime can be included in future models for molecules other than H_2 and CO where it may have a crucial role to play.

1.4.2 Partition function

To calculate the fractional occupation number x_i , partition function $Z(T)$ is defined as:

$$Z(T) = \sum_i g_i e^{-E_i/k_B T}, \quad (3)$$

$Z = Z(T)$, i.e., it is function of temperature.

Then, x_i can be computed as:

$$x_i = \frac{1}{Z(T)} g_i e^{-E_i/k_B T}, \quad (4)$$

This is valid for LTE only.

1.4.3 Line Emission and Absorption - Einstein Coefficients

If an atom or molecule jumps from one energy level to another by absorbing or emitting a photon, the transition is called a *radiative transition*, or a spectral line transition. This means that the radiative transfer equation has to be solved :

$$\frac{dI_\nu}{ds} = j_\nu - \alpha_\nu I_\nu, \quad (5)$$

where j_ν and α_ν are due to this radiative transition.

For two levels i and j , such that $E_i > E_j$, the energy difference between the levels is given by:

$$h\nu_{ij} = E_i - E_j \quad (6)$$

The spontaneous radiative decay j_ν is given as:

$$j_\nu = \frac{h\nu_{ij}}{4\pi} n_i A_{ij} \phi_{ij}(\nu), \quad (7)$$

where:

$$\begin{aligned} n_i &= nx_i, \\ \phi_{ij}(\nu) &= \text{Line profile function, discussed in section 1.4.4,} \\ A_{ij} &= \text{Einstein A-coefficient for this transition in } s^{-1} \end{aligned}$$

Similarly, the extinction coefficient α_ν is given as:

$$\alpha_\nu = \frac{h\nu_{ij}}{4\pi} (n_j B_{ji} - n_i B_{ij}) \phi_{ij}(\nu), \quad (8)$$

where:

$$\begin{aligned} B_{ij} &= \text{Einstein B-coefficient for extinction,} \\ B_{ji} &= \text{Einstein B-coefficient for stimulated emission.} \end{aligned}$$

The Einstein coefficients are related to one another as:

$$A_{ij} = \frac{2h\nu_{ij}^3}{c^2} B_{ij}, \quad B_{ji} g_j = B_{ij} g_i, \quad (9)$$

These are called Einstein Relations. They must apply in order to conserve a thermal Boltzmann distribution (equation 2) in the presence of a Planckian radiation field at the same temperature.

1.4.4 Line profile function ($\phi_{ij}(\nu)$)

$$h\nu_{ij} = E_i - E_j$$

Due to various line broadening effects, the photon that is absorbed or emitted does not have to be exactly at the frequency (ν_{ij}). Instead, a function ϕ_ν is defined that describes the susceptibility of the transition to photons of frequency (ν).

The frequency is normalised as $\int_0^\infty \phi_{ij}(\nu) d\nu = 1$, has maximum at $\nu = \nu_{ij}$ and drops off for $\nu < \nu_{ij}$ and $\nu > \nu_{ij}$.

The line profile function is written here as a Gaussian :

$$\phi_{ij}(\nu) = \sqrt{\frac{2}{\pi}} \frac{1}{\Delta\nu_{ij}} \exp\left(-\frac{(\nu - \nu_{ij})^2}{2\Delta\nu_{ij}^2}\right), \quad (10)$$

where $\Delta\nu_{ij}$ is the line width in Hz.

There can be different models for the computation of the line width $\Delta\nu_{ij}$. The simplest one is the *thermal line broadening*. In this case the line broadening is caused by the thermal motion of the gas particles, then, $\Delta\nu_{ij}$ is given by the isothermal sound speed of the atomic or molecular species, i.e.,

$$\Delta\nu_{ij} = \nu_{ij} \frac{c_s}{c}, \quad (11)$$

where

$$c_s = \sqrt{\frac{k_B T}{m}}$$

is the isothermal sound speed of the atomic or molecular species at $T = \bar{T} = 10\text{K}$, and m is the mass of the species.

Another source of randomised line broadening can be *micro-turbulence* or *sub-grid turbulence*. *Turbulence* is the phenomenon of pseudo-randomly moving parcels of the fluid on the top of some average large scale flow pattern. *Sub-grid turbulence* is the turbulence on the spatial scales smaller than the smallest grid size, This small-scale turbulence must be treated as a velocity dispersion.

$$\Delta\nu_{ij} = \nu_{ij} \frac{\Delta v}{c}, \quad (12)$$

where Δv is the turbulent velocity dispersion in the volume element under consideration, such that:

$$\Delta v = \sqrt{\frac{2}{3} \langle v_{turb}^2 \rangle_{3D}}$$

1.4.5 Photon escape probability and optical depth

In line transfer energy (or photons) can be transported via the lines. But if the optical depth is very large in all the lines that are appreciably emitting light, then the transport of the energy is hampered substantially. It is then useful to look at the various ways by which radiation can nevertheless escape.

One method by which photons can escape is the Sobolev method[8]. The idea here is that a photon can escape from the line due to differences in velocity of gas parcels along the line of sight of the observer. These differences in velocity are caused by turbulence - the higher the turbulence, more easily the photon can escape. If there is no turbulence, then these differences in velocity are caused by the thermal motion of the molecules. This causes a Doppler shift in the emitted photon. If this Doppler shift is larger than the local line width, then the photon suddenly finds itself “free” because the opacity is then suddenly very low as a result of the line having been Doppler shifted away from the frequency of the photon.

$$\tau_{ij} = \frac{h\nu_{ij} n L}{4\pi\Delta\nu_{ij}}(x_j B_{ji} - x_i B_{ij}), \quad (13)$$

where $\Delta\nu_{ij}$ is the line width calculated either by line broadening due to thermal motion of molecules or by considering sub-grid turbulence, and L is the length of the absorbing layer, and this absorbing layer the atoms/molecules are moving with random velocities. [8]

The probability of a photon to escape from a cloud with optical depth τ_{ij} is: [8]

$$\beta_{ij} = \frac{1 - e^{-\tau_{ij}}}{\tau_{ij}} \quad (14)$$

where τ_{ij} is computed on the peak absorption frequency of the line. The idea here is that a photon is emitted from the volume, and then it tries to escape. But to escape it has to not get absorbed by the gas between the emission point and the observer. And the probability of this photon to escape and reach the observer is given by β_{ij} .

This project deals with studying and understanding and then constraining the microscopic properties of the molecules to see their effect on the macroscopic properties of a GMC. This report is structured as follows. The outline of the sub-grid model along with a simplified model for radiative transfer is explained in Section 2. In Section 3, the results of this model are presented. Section 4 details the application of this model to post-process a

sample cosmological galaxy simulation and computation of the CO emission. Conclusions are drawn in Section 5.

2 Model Outline

2.1 Some definitions

2.1.1 Different scales in the model

There are three scales/regimes in the model. The first one is the macroscopic length scale, where macroscopic can be a cloud or a clump. The second scale is the microscopic length scale, where the particles inside the volume element are moving in random directions due to thermal motion. The third scale is the mesoscopic scale, which are between the macroscopic and microscopic scales, and are usually unresolved. And these scales are described by a "sub-grid" mathematical model presented in this report. "Sub-grid" here means inside the volume element.

2.1.2 Turbulence

Turbulence is the phenomenon of randomly moving parcels of the fluid on the top of some average large scale flow pattern, and their random motion is usually caused by the thermal motion of particles.

2.1.3 Sonic Length

This is the size of the density fluctuations inside the density field of this sub-grid model. Below the sonic length scale, the density fluctuations become very weak. The sonic scale can be defined using Burgers Turbulence spectrum:

$$\Delta v(\ell_s) = \Delta v_{turb}^{1D} \sqrt{\frac{\ell_s}{\Delta x}} \quad (15)$$

where $\Delta v(\ell_s) = c_s$, where c_s is the isothermal sound speed of the gas,

$$\ell_s = \frac{\Delta x}{\mathcal{M}^2}$$

, where \mathcal{M} the cell Mach number defined by

$$\mathcal{M} = \frac{\Delta v_{turb}^{1D}}{c_s}$$

2.2 Density field of the sub-grid model

Fragmentation of gas clouds has been intensively studied in the past, and both numerical and analytical models [9][10] have shown that the density field of an isothermal, non-gravitating, turbulent gas of mean number density \bar{n}_H is well described by a log-normal Probability Distribution Function (PDF). The volume-weighted PDF ($P_V(s)$) can be written as:

$$P_V(s) = \frac{1}{(2\pi\sigma_s^2)^{1/2}} \exp \left[-\frac{1}{2} \left(\frac{s - \bar{s}}{\sigma_s} \right)^2 \right], \quad (16)$$

where:

$$s = \ln(n_H/\bar{n}_H), \quad (17)$$

$$\bar{s} = -\sigma_s^2/2, \quad (18)$$

where s is the sonic length density element, \bar{n}_H is the mean number density of the cloud, \bar{s} is related to the volume-averaged value of the logarithm of the density *References from Paper-1*. σ_s depends on the sonic Mach number (\mathcal{M}) as:

$$\sigma_s^2 = \ln(1 + b^2 \mathcal{M}^2), \quad (19)$$

where b parameterises the kinetic energy injection mechanism driving the turbulence. In this model $b = 0.3$ everywhere.

2.3 Length scale of the absorbing layer

The sonic length density element is defined by the PDF in equation 16. To know what the absorbing length of this density element will be, the well known Jeans instability criterion is used.

For an isothermal, non-magnetic, non-rotating sphere of gas, the critical wavelength of a perturbation is given by: [11]

$$\lambda_J = \frac{c_s}{\sqrt{4\pi G n_H m_p}}, \quad (20)$$

where m_p is the mass of a proton, and c_s is the isothermal sound speed of the gas given as:

$$c_s = \sqrt{\frac{k_B T}{m_p}} \quad (21)$$

In this model, $T = \bar{T} = 10\text{K}$, which is the general average temperature of a cloud.

The onset of the dynamical collapse of a self-gravitating cloud requires the specification of the initial conditions. In the early models ([11]) these initial conditions were assumed to be due to thermal and gravitational effects only. This means that the self-gravitating clumps will have a critical length scale, which is the well-known Jeans length.

The Jeans length is a common approximation to calculate the absorbing length, with the physical justification that at the centre of a gravitationally collapsing core, the radiative background will be attenuated by a column of gas with a length-scale approximately equal to λ_J [12].

In the framework of this model, Jeans length depends on the density of the cloud. So each clump inside the cloud will have a different density given by equation 16 and each of these clumps will then have a corresponding Jeans length. This means that clumps with sizes smaller than the Jeans length will not collapse, they will either diffuse away or stay like that. In contrast, clumps with sizes larger than Jeans length will collapse and disappear. This means that the only clumps emerging out of these densities are ones with size corresponding to that of the Jeans length, because those are the clumps that are on the onset of collapse [12].

2.4 Power-law PDF due to self-gravity

For supersonic non-gravitating turbulent isothermal gas, the density PDF is log-normal [13][14][15]. But when density increases and self-gravity becomes important, more and more denser clumps start to form. This increase in probability of finding denser clumps results in developing a power-law tail on the high-density side of the PDF [13][16][17]. Recent observation of column density PDF support these theoretical predictions [13][18][19].

In this model the evolution of density PDF is defined based on a free-fall collapse via the formalism developed by Girichidis et. al [13]. Assuming a pressure-free collapse, these authors provide a set of analytical equations to calculate the functional form of the PDF at any given time, $P_V(s, t)$, given the initial $P_V(s, 0)$.

As the initial PDF, $P_V(s, 0) \equiv P_V(s)$, where $P_V(s)$ is defined in equation-16. Defining γ such that

$$\gamma = \frac{1 + 2\epsilon \exp(s) - \sqrt{1 + 4\epsilon \exp(s)}}{2\epsilon^2 \exp(s)}, \quad (22)$$

where $\epsilon = 0.4$. Now the density as a function of time can be explicitly computed:

$$s' = \ln \gamma, \quad (23)$$

Defining the bin-width q in terms of density and time:

$$q = \frac{[1 - \epsilon \exp(s')]^3}{1 + \epsilon \exp(s')}, \quad (24)$$

The new PDF can be computed as

$$P'_V(s) = q P_V(s) \quad (25)$$

Re-normalising $P'_V(s)$ by total enclosed mass to get the final 'evolved'-PDF $P_V(s, t)$:

$$P_V(s, t) = \frac{P'_V(s)}{\int \exp(s) P'_V(s) ds} \quad (26)$$

2.5 H_2 formation model

As discussed in section 1.3, the background UV radiation from young stars commonly known as far-UV (FUV) radiation, is responsible for breaking apart molecules into their constituent atoms, a process called photo-dissociation. This phenomenon is balanced by the formation of molecules on the surface of dust grains when the dust accumulates in the clump and blocks the FUV radiation from seeping in. This balance between formation of molecules on the surface of dust grains and the destruction of molecules by the FUV flux is given by the chemical rate equation that controls the abundances of the molecules. In equilibrium, the creation rate (CR) of molecules will be equal to the destruction rate (DR) of the molecules.

For H_2 ,

$$CR = k Z n_{\text{HI}} n_H, \quad (27)$$

$$DR = c \sigma_{\text{dust}} n_{H2} n_{\text{LW}}, \quad (28)$$

where k is the creation coefficient, such that $k = 2.5 \times 10^{-17} \text{ cm}^3 \text{s}^{-1}$, Z is the metallicity of the cloud in solar units, σ_{dust} is the mean cross-section of the dust particles, n_{HI} is the number density of H atoms, n_{H2} is the number

density of H_2 molecules, and n_{LW} is the number of photo-dissociating Lyman-Werner (LW) photons. n_{HI} and n_{H2} are related to n_H as:

$$n_H = n_{HI} + 2n_{H2}, \quad (29)$$

In equilibrium, the creation and destruction rates are equal. Equating equations 27 and 28, and using equation 29:

$$n_H = \left(\frac{c \sigma_{dust} n_{H2} n_{LW}}{k Z n_H} + 2 \right) n_{H2}, \quad (30)$$

This gives the molecular fraction X_{H_2} of H_2 :

$$X_{H_2} = \frac{n_{H2}}{n_H} = \frac{1}{2 + \left(\frac{c \sigma_{dust} n_{H2} n_{LW}}{k Z n_H} \right)}, \quad (31)$$

Here, the number of photo-dissociating LW photons n_{LW} is computed as:

$$n_{LW} = (ISRF) e^{-\tau_{LW}}, \quad (32)$$

where τ is the optical depth in the Lyman-Werner (LW) band due to dust given by:

$$\tau_{LW} = 1000 m_p Z n_H \lambda_J, \quad (33)$$

In this model, $ISRF$ is the Inter-Stellar Radiation Field, or the FUV flux, in units of G_0 , where G_0 is the Habing flux in the Solar neighbourhood. Young, massive stars are the main source of the FUV photons which permeate the ISM and readily photo-dissociate interstellar molecules, such as H_2 and CO . This model does include an H_2 -dissociating FUV photo-background, though assumed it to be constant in both space and time. ($G_0 = 1(Solar)$)

2.6 Self Shielding of H_2

As detailed in section 1.3, dust plays a huge role in blocking FUV radiation to allow formation of H_2 . Such an approximation is appropriate for sufficiently low column densities of molecular gas. However, for higher densities, gas also 'self-shields' in addition to dust, i.e., in regions where H_2 column densities $N_{H_2} \geq 10^{21} \text{cm}^{-2}$, photo-dissociation by FUV photons becomes suppressed. This is because as density increases, the optical depth for

the photons also increases, which means that the gas becomes optically-thick for photo-dissociating LW photons [2] [3].

Self-shielding of molecular hydrogen has been studied extensively since the pioneering work of Stecher and Williams [4]. A commonly used formula that conveniently parameterises the self-shielding effects for H₂ with (local) one-dimensional velocity dispersion was given by Draine and Bertoldi [3],

$$S_{H_2} = \frac{0.965}{(1 + x/b_5)^2} + \frac{0.035}{\sqrt{1+x}} \exp\left(-\frac{\sqrt{1+x}}{1180}\right) \quad (34)$$

where $x \equiv N_{H_2}/5 \times 10^{14} \text{ cm}^{-2}$, and $b_5 \equiv b_0/\text{km/s}$, where $b_0 = \sqrt{2}\Delta v$, but here in this model $b_0 = 1\text{km/s}$ is used.

Here N_{H_2} is the column density of H₂ given in this model as:

$$N_{H_2} = n_{H_2} \lambda_J \quad (35)$$

The accuracy of this shielding function has been confirmed by Sternberg et al.[20] who also explicitly accounted for line overlap in the LW bands, and by Gnedin and Draine [2].

Including this effect in the model,

$$n_{\text{LW,SS}} = G_0 S_{H_2} \exp(-\tau_{\text{LW}}), \quad (36)$$

$$X_{H_2,SS} = \frac{1}{2 + \left(\frac{c \sigma_{\text{dust}} n_{H_2} n_{\text{LW,SS}}}{k Z n_H}\right)}, \quad (37)$$

$$n_{H_2,SS} = n_H X_{H_2,SS}, \quad (38)$$

where $n_{\text{LW,SS}}$ is the number of photo-dissociating LW photons, $X_{H_2,SS}$ is the molecular fraction, and $n_{H_2,SS}$ is the number density of H₂ molecules calculated by considering self-shielding of H₂. Here, in $n_{\text{LW,SS}}$, S_{H_2} is computed using n_{H_2} for the first iteration. Then $X_{H_2,SS}$ and $n_{H_2,SS}$ are calculated. After the first iteration, S_{H_2} is computed using $n_{H_2,SS}$, and then again $n_{\text{LW,SS}}$, $X_{H_2,SS}$ and $n_{H_2,SS}$ are computed. In the third iteration, S_{H_2} is computed using $n_{H_2,SS}$ from the second iteration, and so on and so forth. This iterative process is carried out 15 times to reach a converging value for the self-shielding variables.

2.7 CO formation model

Significant CO fractions only form in the densest regions of the gas where a combination of dust, H₂, and self-shielding attenuates the FUV background.

The molecular fraction X_{CO} and the number density n_{CO} of CO can now be computed as:

$$X_{CO} = \frac{1}{1 + \frac{\Gamma_{CO}}{n_{H_2} k_0 \zeta}}, \quad (39)$$

$$n_{CO} = 10^4 \times Z n_H X_{CO}, \quad (40)$$

where, $\zeta = \left\{ 1 + \frac{\Gamma_{CHX}}{n_H k_1 k_2} \right\}^{-1}$,

$\Gamma_{CO} = 10^{-10} n_{LW}$ and $\Gamma_{CHX} = 5 \times 10^{-10} n_{LW}$ are the different destruction rates of CO calculated using the number of LW photons, and k_0, k_1, k_2 are constants [21].

The results for CO given by this model are accurate enough to not consider self-shielding of CO , meaning X_{CO} and n_{CO} are computed using n_{LW} , X_{H_2} , and n_{H_2} .

One necessary feature to include in the model is the temperature and mean density cut-off. All the volume elements with $T > 10^4 K$ or $\overline{n_H} < 10^{-2} cm^{-3}$ are not taken into account while computing the molecular fractions. This is because at temperatures $T > 10^4 K$, H will be collisionally-ionised, so there will no formation of H_2 and CO . And at mean cell densities $\overline{n_H} < 10^{-2} cm^{-3}$, H will be photo-ionised by the background FUV flux, and so there will be no formation of H_2 and CO .

2.8 Line radiative transfer

A simplified routine for line radiative transfer is adopted in this model.

The total number of energy levels (N_{tot}), energy (E_i) & statistical weight (g_i) for each energy level, frequencies of transitions between different energy levels (ν_{ij}), and the Einstein-A coefficient (A_{ij}) for CO are all read from the from the Leiden Atomic and Molecular Database (LAMDA) file [5]. Einstein-B coefficients (B_{ij} and B_{ji}) are calculated using equation 9.

Then, using N_{tot} , E_i and g_i from the LAMDA file, and using $T = \overline{T} = 10K$, the partition function (Z) and fractional occupation number (x_i) for CO are calculated using equation 3 and 4 respectively.

In this sub-grid model, only the first CO transition is considered, i.e., the transition from the first excited state to the ground state. Which means that $i = 1$ and $j = 0$. Also, $n \equiv n_{CO}$.

Integrating equation 7 over the frequency and solid angle, the integrated emissivity of $CO(1 - 0)$ transition line is obtained:

$$j_{10} = h\nu_{10} n x_1 A_{10} \quad (41)$$

Using j_{10} , and photon escape probability β_{10} computed from equation 14, the luminosity density of the $CO(1 - 0)$ transition line can be calculated as:

$$\ell_{CO} = j_{10}\beta_{10} \quad (42)$$

Then, the α_{CO}^{-1} factor can be defined as:

$$\alpha_{CO}^{-1} = \frac{\ell_{CO}}{n_H} \quad (43)$$

3 Results from the Sub-Grid Model

3.1 Log-normal PDF vs Power-law PDF

Figure 1 shows the comparison between the log-normal PDF described by equation 16 and the power-law PDF described by equation 26. The density of the cloud is plotted on the X-axis against the PDF on the Y-axis. The log-normal PDF is described by assuming that the cloud is non-gravitating. When self-gravity is included in the formalism, the PDF develops a power-law tail in the high density region of the cloud. This is because as the density grows, the probability of finding denser clumps increases. The evolution of this power-law tail is shown in figure 1.

It was found in this model that the power-law PDF didn't affect the computed values by much, i.e., the self-gravity of the gas doesn't play much of a role for H_2 and CO . So, only the log-normal PDF and its effects are considered in this model hereafter. The power-law PDF can be included in future models for molecules other than H_2 and CO where it may have a crucial role to play.

3.2 Length scale of the absorbing layer

As shown in equation 20, $\lambda_J \propto \frac{1}{\sqrt{n_H}}$, i.e., as the density of the cloud increases, the length of the absorbing layer decreases. This is clearly represented in figure 3.

3.3 Molecular fractions of H_2 and CO

Self-shielding of H_2 plays an important role in H_2 and CO formation, as discussed in sections 2.5 and 2.6. If self-shielding of H_2 is not included in the model, the H_2 formation shifts to a much higher critical density. In figures 4a, the number of photo-dissociating LW photons are plotted as a function of the density of the cloud, for both regimes, without self-shielding of H_2 (n_{LW}) and including self-shielding of H_2 ($n_{LW,ss}$).

In the case without self-shielding, the critical density at which H_2 starts forming, i.e., the density at which the cloud becomes optically thick for the LW photons is at $n_{crit} \approx 10^4 \text{ cm}^{-3}$. This is much higher than observed in gas clouds, where $n_{crit} \approx 10^1 - 10^2 \text{ cm}^{-3}$. Now if the self-shielding effects are included, as is shown in figure 4a, the critical density cut-off shifts significantly

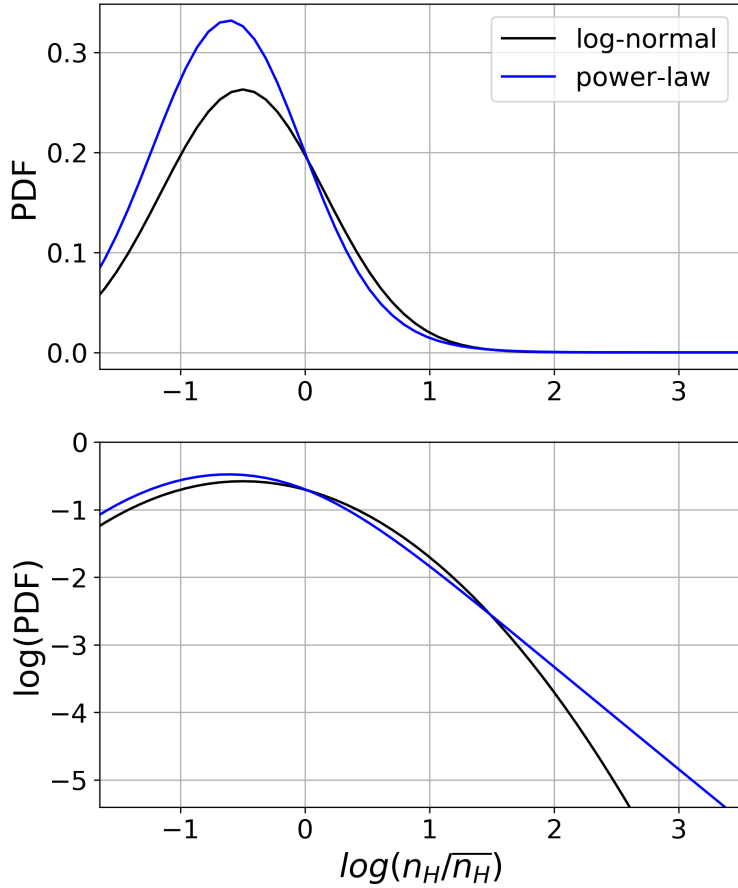


Figure 1: $\log(n_H)$ vs PDF and $\log(\text{PDF})$: Comparing the log-normal PDF and the power-law PDF. The mach number here is $\mathcal{M} = 10$.

to the lower side of the density scale. In this regime, the critical density $n_{crit} \approx 10^1 - 10^2 \text{ cm}^{-3}$, which is in perfect agreement with the observations.

As expected, this shifting of the critical density towards the lower side of the density scale after self-shielding of H_2 is included is mimicked by the molecular fraction of H_2 . In figure 4b, without self-shielding H_2 starts forming at $n_{crit} \approx 10^4 \text{ cm}^{-3}$. But with self-shielding, H_2 starts forming at $n_{crit} \approx 10^1 - 10^2 \text{ cm}^{-3}$, which is again what is observed by astronomers. This proves the significance, and validity, of the self-shielding of H_2 .

Similarly, the molecular fraction of CO is plotted as a function of the density of the cloud in figure 5. For CO , which typically forms at densities higher than H_2 , the critical density given by the model is $n_{crit} \approx 10^4 \text{ cm}^{-3}$. This value is in confirmation with astronomical observations. And since the resulting n_{crit} for CO is accurate enough, self-shielding of CO is not included in the model.

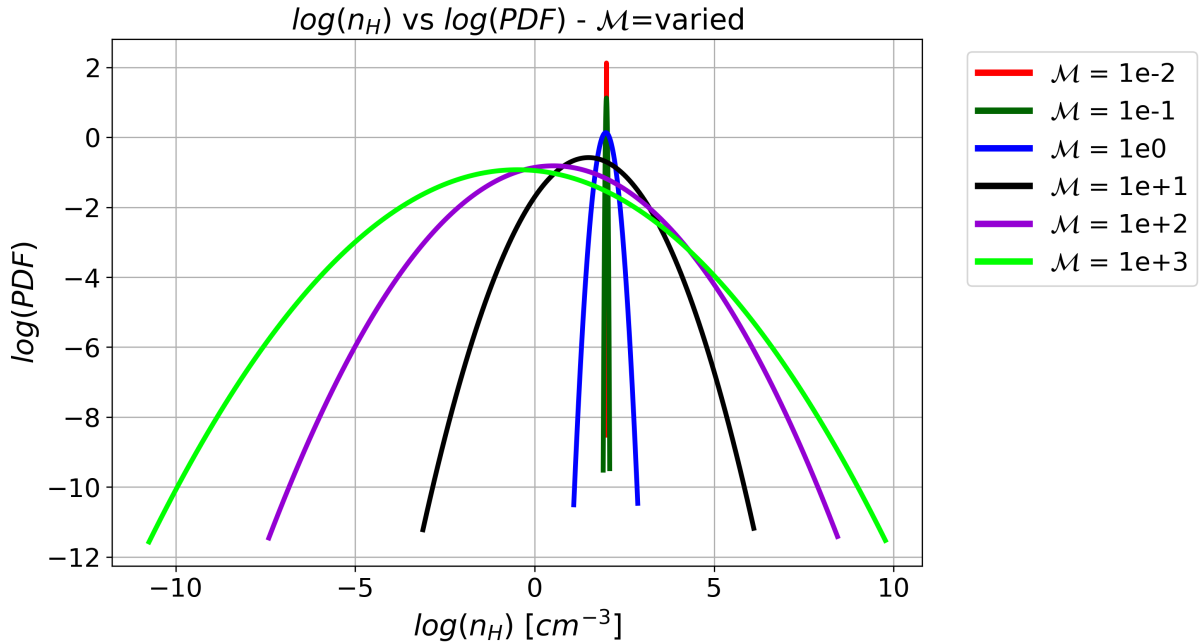


Figure 2: $\log n_H$ vs $\log PDF$: Varying \mathcal{M} for the log-normal PDF. As the Mach number is increased, the PDF expands, i.e., the mass increases. The opposite effect is observed when the Mach number is decreased.

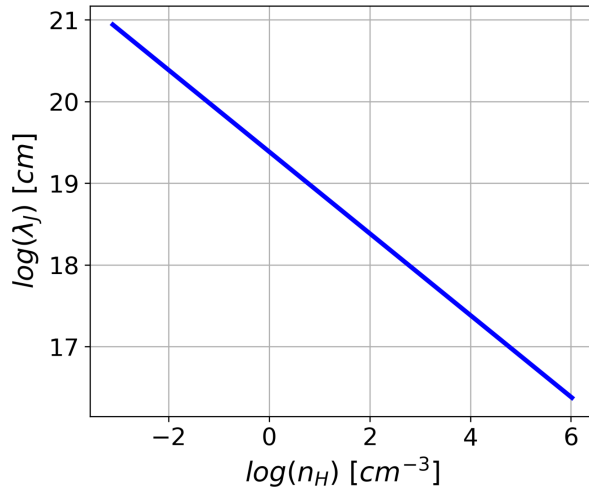
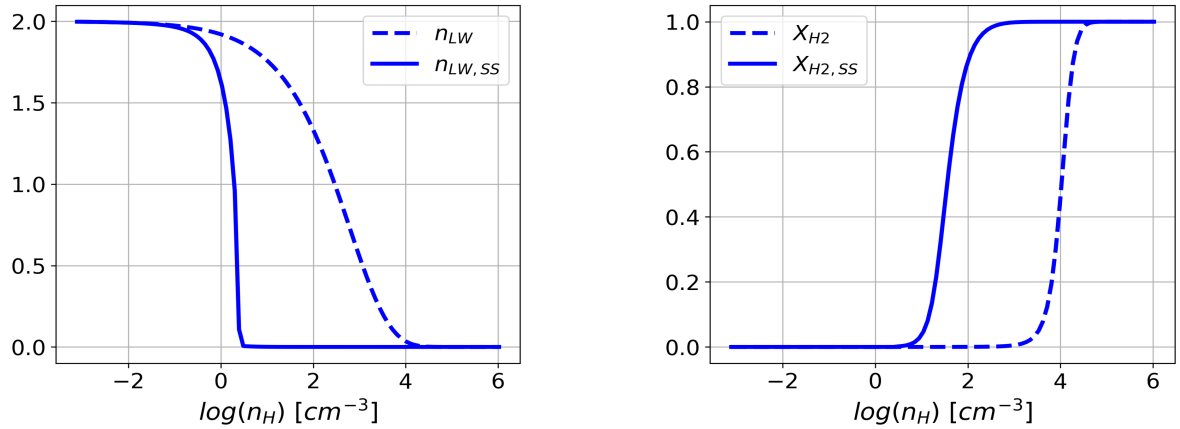


Figure 3: $\log(n_H)$ vs $\log(\lambda_J)$: Plotting the length of the absorbing layer as function of the density of the cloud.

3.4 Line optical depth and luminosity density

As discussed in sections 1.4.4 and 1.4.5, there are two regimes for line broadening - thermal line broadening, and line broadening due to micro-turbulence.

In the regime of thermal line broadening, the isothermal sound speed for



(a) without self-shielding (n_{LW}), and with self-shielding ($n_{LW,ss}$).

(b) without self-shielding (X_{H_2}), and with self-shielding ($X_{H_2,ss}$).

Figure 4: The number of photo-dissociating LW photons and the molecular fraction of H_2 plotted as function of the density of the cloud - with and without self shielding.

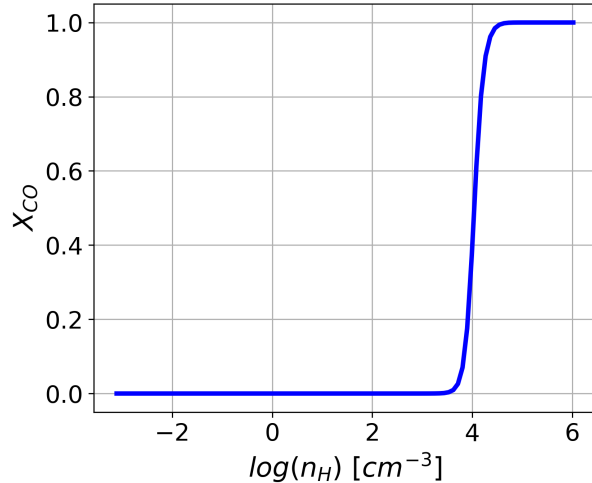
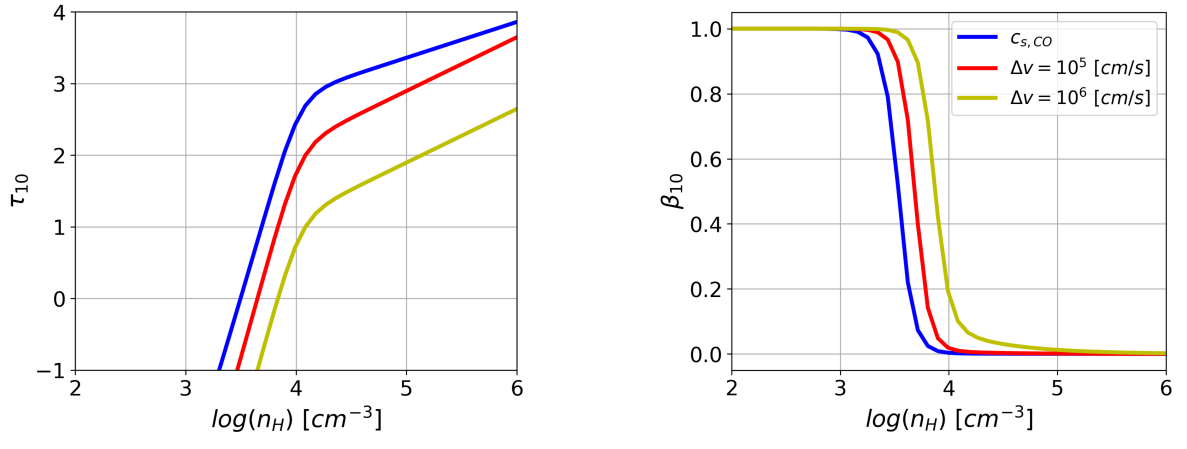


Figure 5: $\log(n_H)$ vs X_{CO} : Molecular fraction of CO plotted as function of the density of the cloud (self-shielding effects for CO not included).

CO is used to calculate the line width $\Delta\nu$. Whereas in the micro-turbulence line broadening regime, the velocity dispersion (Δv) is used to calculate $\Delta\nu$. In figures 6a and 6b, the optical depth and the escape probability for the emitted photons is plotted as a function of the density of the cloud. Three cases are shown - (1) using isothermal sound speed, (2) using velocity dispersion $\Delta v = 10^5 cm/s$, and (3) using velocity dispersion $\Delta v = 10^6 cm/s$.

As seen from the figure 6a, for the case with isothermal sound speed of



(a) line optical depth (τ_{10}) plotted as function of the density of the cloud.

(b) escape probability of the emitted photon (β_{10}) plotted as function of the density of the cloud.

Figure 6: The optical depth and the escape probability for the emitted photons is plotted as a function of the density of the cloud - using isothermal sound speed, and using different values of velocity dispersion Δv .

CO, the optical depth of the emitted photons using the isothermal sound speed is larger than the optical depth using velocity dispersion. This translates into the escape probability in figure 6b, where the critical density for the photon to escape is lower than the for the isothermal sound speed case than the cases considering velocity dispersion.

This phenomenon becomes clearly evident when the α_{CO}^{-1} factor of the line emission of *CO* is plotted as function of density in figure 7. As expected, the factor for the velocity dispersion cases is larger than the factor for the isothermal sound speed case.

The Burgers relation from equation 15 is used to compute the turbulent velocity dispersion:

$$\Delta v = \Delta v_{turb}^{1D}(\lambda_J) = c_s \sqrt{\frac{\lambda_J}{\ell_s}}$$

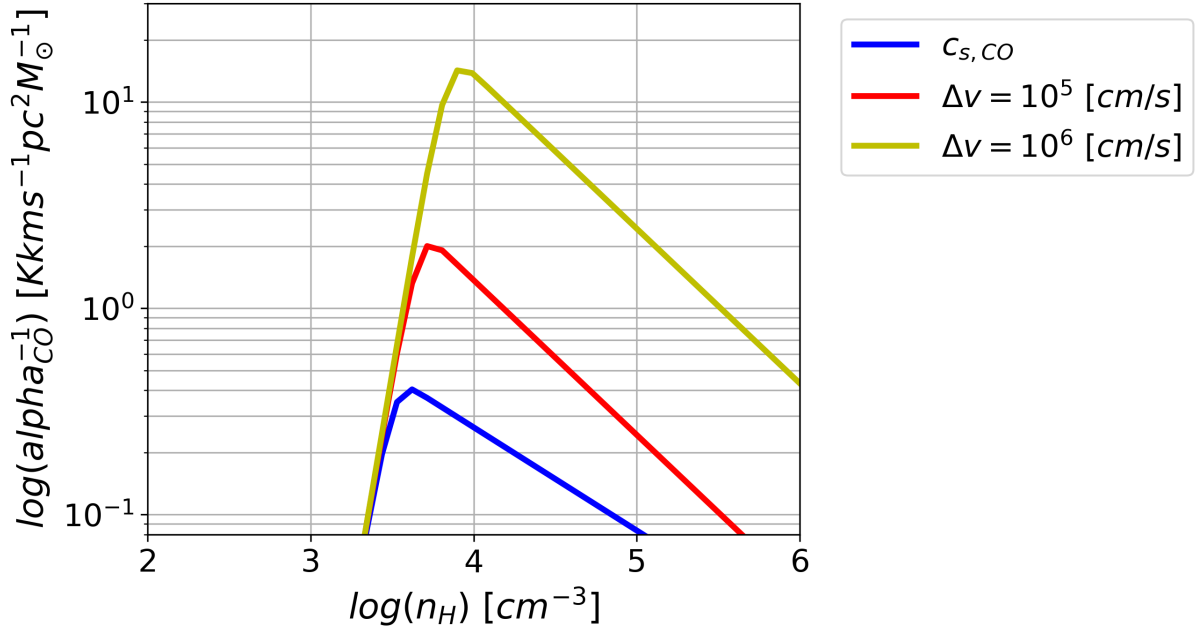


Figure 7: $\log(n_H)$ vs $\log(\alpha_{CO}^{-1})$: the sub-grid α_{CO}^{-1} factor of line emission of CO plotted as function of the density of the cloud - using isothermal sound speed, and using different values of velocity dispersion Δv .

4 Application of the model on a Simulation

4.1 Salient features

The sub-grid model is applied on a cosmological zoom-in hydro-dynamical simulation of a galaxy. The salient features of this simulation are discussed briefly.

The galaxy selected is from an N-body simulation with 512^3 particles in a box size $25h^{-1}\text{Mpc}$. The galaxy has a redshift $z \approx 0.6$, with virial radius $R_{vir} \sim 150\text{kpc}$. The radius of the galactic disk is defined as $0.1 \times R_{vir}$. The virial mass is $M_{vir} = 7.86 \times 10^{11}\text{M}_\odot$. The total stellar mass is $M_\star \sim 1.83 \times 10^{10}\text{M}_\odot$, the mean gas surface density $\langle \sum_{gas} \rangle \sim 31.5\text{M}_\odot/\text{pc}^2$, and the star formation rate is $\text{SFR} \approx 2\text{M}_\odot\text{yr}^{-1}$. The simulation uses separate sub-grid models for turbulence, star formation, and stellar feedback to compute the effective SFR. The computation of SFR is discussed in detail in [22]. For the zoom-in, the maximum resolution was set to $l_{max} = 19$, and the simulation snapshot was refined to reach a minimum cell size of $\Delta x \sim 80\text{pc}$.

The simulation is based on the Adaptive Mesh Refinement (AMR) code RAMSES [23]. AMR is a technique in which the computational space is

divided into smaller cubical cells. The size of each of these simulation cells can be constrained individually on the basis of a parameter of choice. For example, in the case where the parameter of choice is the density, the denser regions (like the galaxy core) will be divided into much smaller cubical cells, and the less dense regions of the galaxy will be divided into larger cubical cells. This allows to adaptively refine the spatial resolution and lower the computation time.

For each of these simulation cells, the macroscopic parameters are - Mach number, metallicity, mean gas number density, temperature, turbulent velocity dispersion, and cell size. Each of these parameters are different for each simulation cell. Mach number for each cell in the simulation is calculated as:

$$\mathcal{M} = \frac{\Delta v}{c_s} \quad (44)$$

where Δv is the velocity dispersion of the turbulence in each simulation cell, and c_s is the isothermal gas sound speed for each simulation cell computed using the temperature of each simulation cell.

The sub-grid model is applied on each of these cubical cells to resolve the microscopic scales in the simulation. For each of the simulation cell, the parameters are sent to the sub-grid model to compute the mean molecular fractions of H_2 and CO , and also the mean line luminosity density of CO . For each simulation cell, the mean values are computed as:

$$\overline{X_{H_2}} = \int X_{H_2,ss} \exp(s) P_V(s) ds, \quad (45)$$

$$\overline{X_{CO}} = \int X_{CO} \exp(s) P_V(s) ds \quad (46)$$

$$\overline{\ell_{CO}} = \int \ell_{CO} P_V(s) ds \quad (47)$$

$$\overline{\alpha_{CO}^{-1}} = \frac{\overline{\ell_{CO}}}{\overline{n_H}} \quad (48)$$

where

$$s = \ln \left(\frac{n_H}{\overline{n_H}} \right)$$

The mean luminosity density is then summed over all the simulation cells to obtain the total luminosity of the galaxy L_{CO} , such that:

$$L_{CO} = \sum_{cells} \overline{\ell_{CO}} (\Delta x)^3 \quad (49)$$

The total H_2 mass in the galaxy can be computed as:

$$M_{H2} = m_p \sum_{cells} \overline{X_{H_2}} \overline{n_H} (\Delta x)^3 \quad (50)$$

Then, the mean $\overline{\alpha_{CO,TOT}^{-1}}$ factor can be computed as:

$$\overline{\alpha_{CO,TOT}^{-1}} = \frac{L_{CO}}{M_{H2}} \quad (51)$$

4.2 Model Predictions

The sub-grid model will be applied on each cubical cell of the simulation. For each simulation cell there is single value for these parameters: $\overline{X_{H_2}}$, $\overline{X_{CO}}$, $\overline{\ell_{CO}}$, $\overline{\alpha_{CO}^{-1}}$, \mathcal{M} , Z , Δv and $\overline{n_H}$. As shown, values such as PDF, λ_J , n_{LW} , β_{10} , j_{10} , etc. are all properties of the cloud inside the simulation cell, whereas \mathcal{M} , Z , Δv and $\overline{n_H}$ are properties of each cell of the simulation.

But before applying the model on the simulation, the model itself can be used to predict the results that will be obtained from post-processing the simulation. This can be done by varying the parameters that control macroscopic properties of the simulation cell (\mathcal{M} , Z , G_0 , Δv , $\overline{n_H}$). If these parameters are varied in steps, and for each such iteration the sub-grid model computes $\overline{X_{H_2}}$, $\overline{X_{CO}}$, $\overline{\alpha_{CO}^{-1}}$, it can effectively mimic the grid of values that will be obtained after post processing the simulation.

In the following figures, $\overline{X_{H_2}}$, $\overline{X_{CO}}$, $\overline{\alpha_{CO}^{-1}}$ are plotted against the mean density $\overline{n_H}$ (given by each iteration) by controlling and varying \mathcal{M} , Z , G_0 one-by-one in succession.

At high \mathcal{M} , the PDF gets wider, meaning that there is more mass at higher cloud densities, as depicted in figure 2. The light green curve in the figure 8 corresponds to a very high Mach number, which corresponds to a lot of mass at very high densities where H_2 forms more easily. That is why there is more H_2 corresponding to a higher Mach number for a given mean cell density ($\overline{n_H}$) than for a smaller value of the Mach number. A similar trend is reproduced in the case of CO in figure 9 where more CO forms at higher \mathcal{M} -values for a given mean cell density.

Metallicity corresponds to the fraction of heavier elements found in the cell. Higher the metallicity, more metal-rich the cell will be. A more metal-rich cell will mean that the gas will be optically thick at much lower mean cell density ($\overline{n_H}$). This would result in more H_2 formation, which can be seen

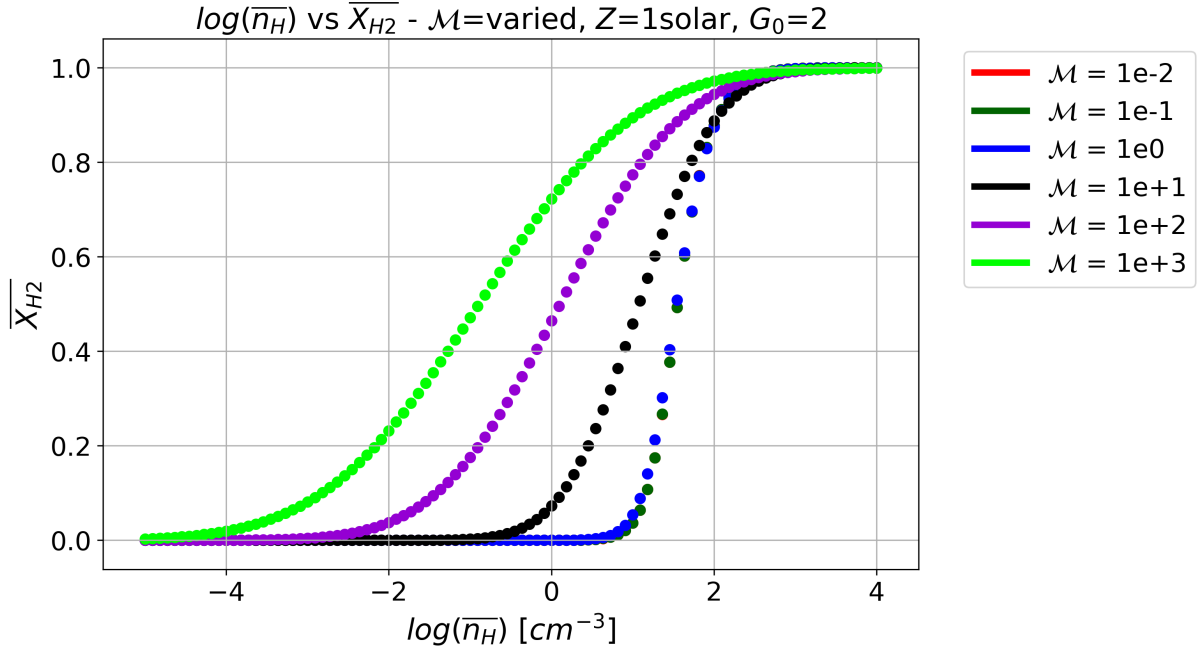


Figure 8: \overline{X}_{H_2} vs \overline{n}_H : Varying \mathcal{M} - Model prediction.

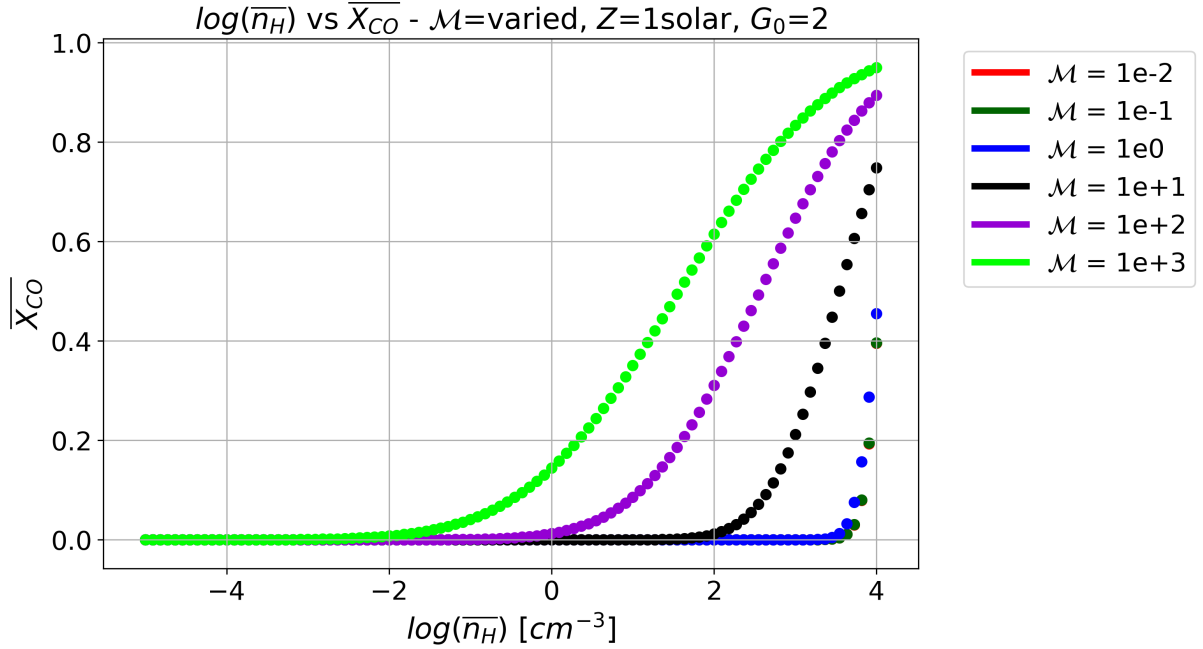


Figure 9: \overline{X}_{CO} vs \overline{n}_H : Varying \mathcal{M} - Model prediction.

in figure 10. The light green curve corresponds to higher metallicity, which corresponds to more H_2 formation at a given mean cell density than for a smaller values of metallicity. A similar trend is reproduced in the case of CO in figure 11 where more CO forms at higher Z -values for a given mean cell

density.

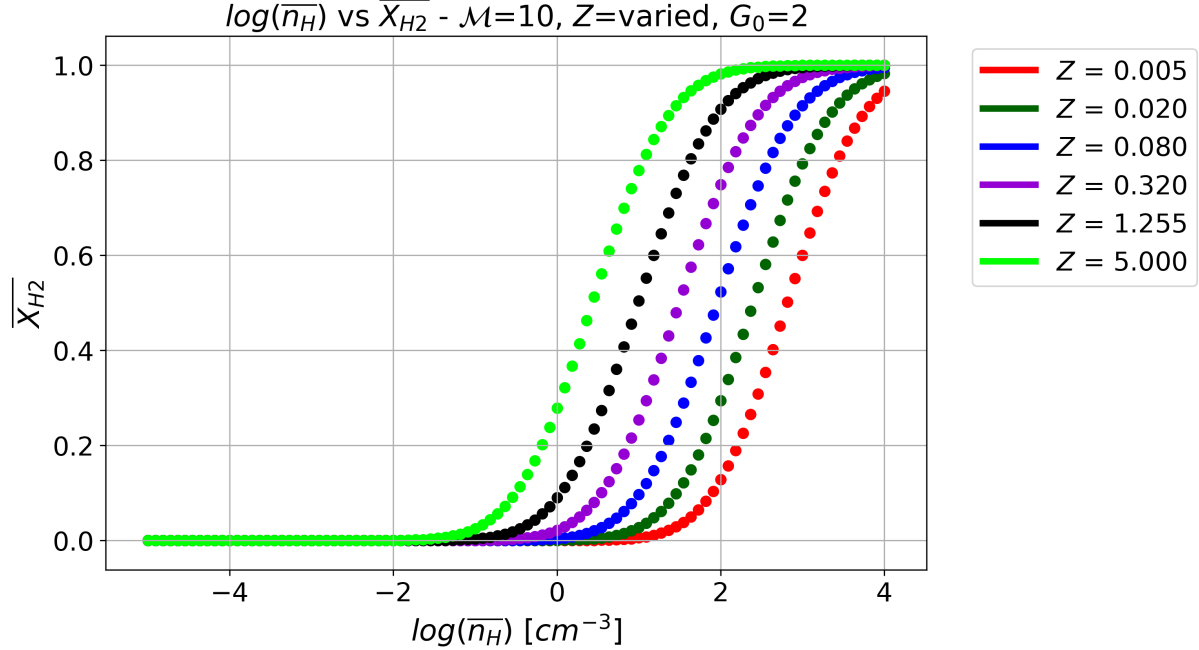


Figure 10: $\overline{X_{H_2}}$ vs $\overline{n_H}$: Varying Z - Model prediction.

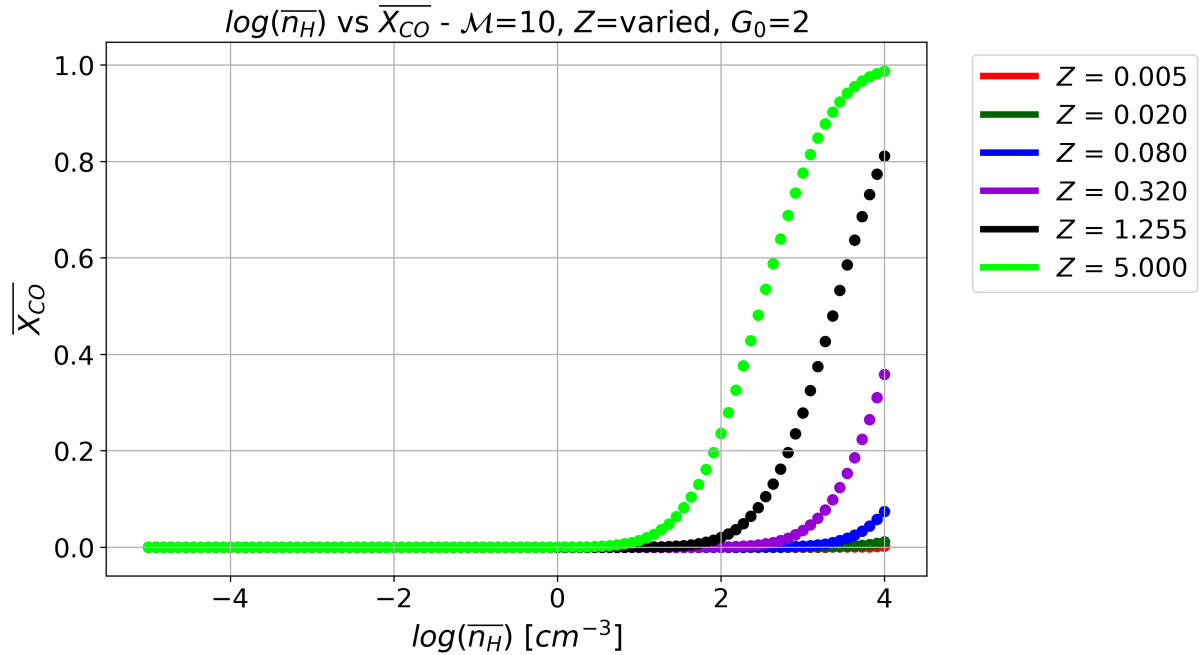


Figure 11: $\overline{X_{CO}}$ vs $\overline{n_H}$: Varying Z - Model prediction.

G_0 is a measure of ISRF, which is responsible for destruction of H_2 through photo-dissociation. Higher values of G_0 mean that more H_2 molecules

will be broken apart via photo-dissociation due to the background UV radiation. Lesser G_0 means less photo-dissociation and more formation of H_2 . This is shown in figure 12. The light green curve corresponds to highest background UV flux. For such large G_0 -values, there is less H_2 at a given mean cell density than for smaller values of G_0 . A similar trend is reproduced in the case of CO in figure 13 where less CO forms at higher G_0 -values for a given mean cell density.

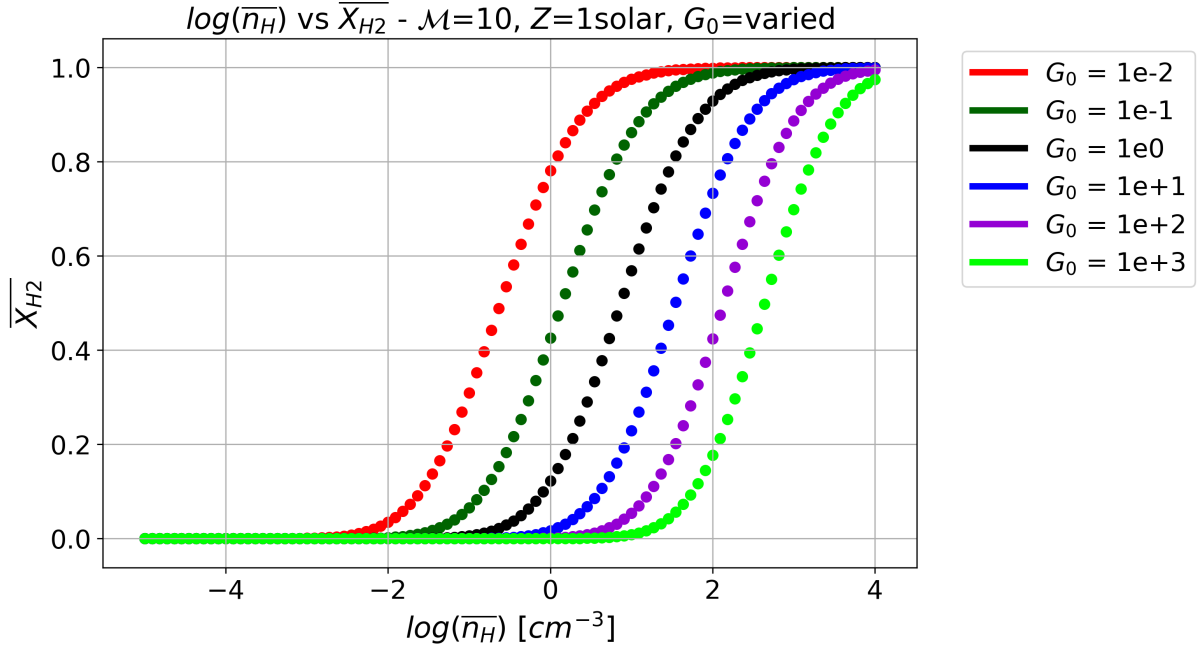


Figure 12: $\overline{X_{H_2}}$ vs $\overline{n_H}$: Varying G_0 - Model prediction.

The mean $\overline{\alpha_{CO}^{-1}}$ factor is plotted as a function of mean cell density $\overline{n_H}$ in figure 14. As can be observed, $\overline{\alpha_{CO}^{-1}}$ for $\Delta v = 10^6 \text{ cm/s}$ is the largest, followed by $\Delta v = 10^5 \text{ cm/s}$ and then $c_{s,CO}$. This proves that more turbulent the cell is, the more easily the emitted photon can escape. For isothermal sound speed $c_{s,CO}$, the relative motions of the volume elements in the cell were not large, so most of the emitted photons got absorbed. But for $\Delta v = 10^6 \text{ cm/s}$, the turbulent motions of volume elements in the cell allowed more number of emitted photons to escape, thus giving a higher value for $\overline{\alpha_{CO}^{-1}}$.

4.3 Applying the sub-grid model on the simulation

The sub-grid model is applied on the simulation to study the behaviour of the gas and the relation between the microscopic and macroscopic properties

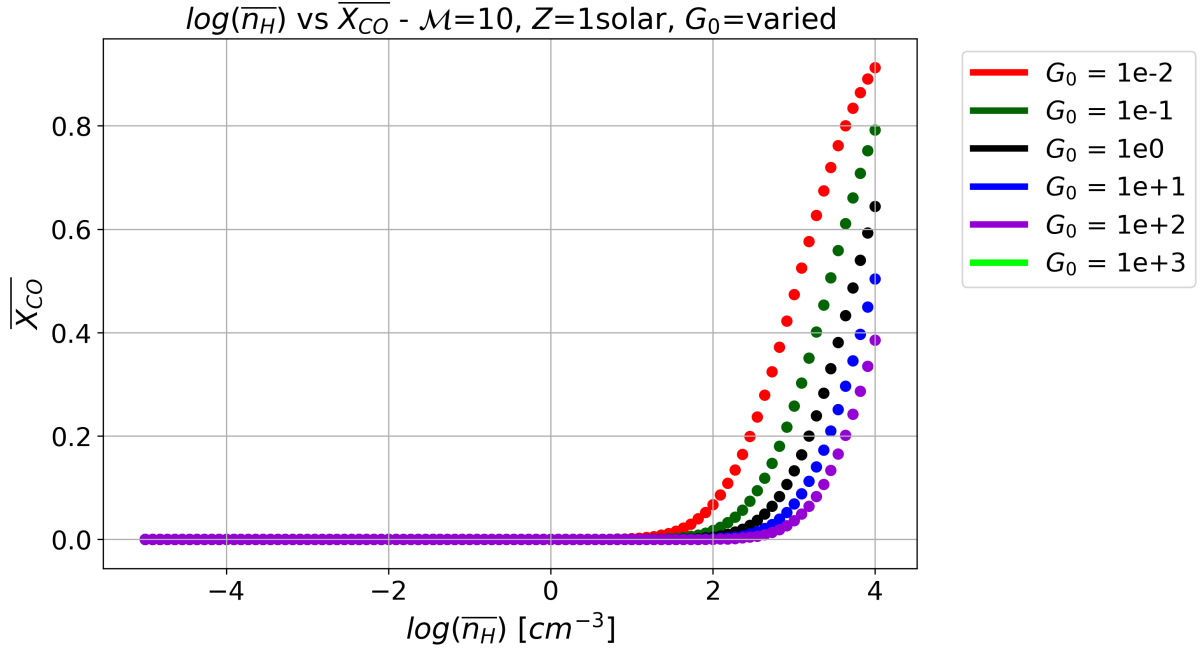


Figure 13: \bar{X}_{CO} vs \bar{n}_H : Varying G_0 - Model prediction.

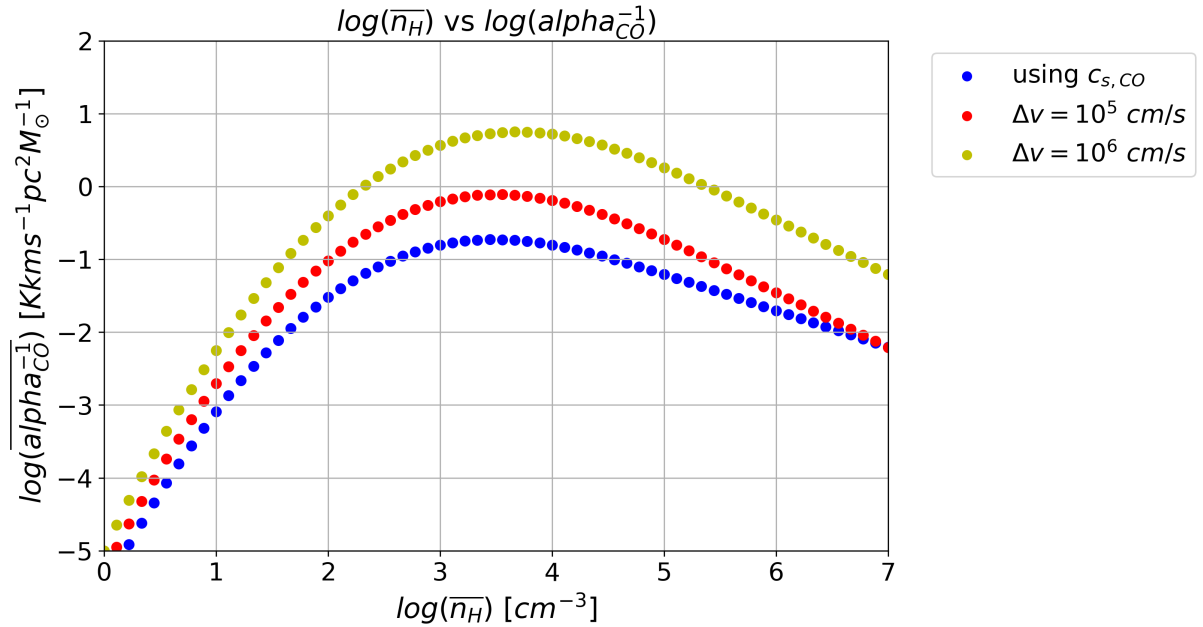


Figure 14: $\log(\bar{\alpha}_{CO}^{-1})$ vs \bar{n}_H : for $c_{s, CO}$ and Δv - Model prediction.

of the galaxy. Mean cell quantities, i.e., \bar{X}_{H_2} , \bar{X}_{CO} , $\bar{\alpha}_{CO}^{-1}$ which are computed using the sub-grid model on each simulation cell, are plotted against the mean cell density of the simulation cell \bar{n}_H , and their behaviour for different Mach numbers and metallicities is studied.

There is one assumption while applying the sub-grid model on the simulation: All the gas in the simulation is subjected to the same amount of background FUV flux in units of G_0 . This is because including a model with a comprehensive FUV background will require full-scale radiative transfer models that were beyond the scope of this project. This feature can be considered in future iterations of the project.

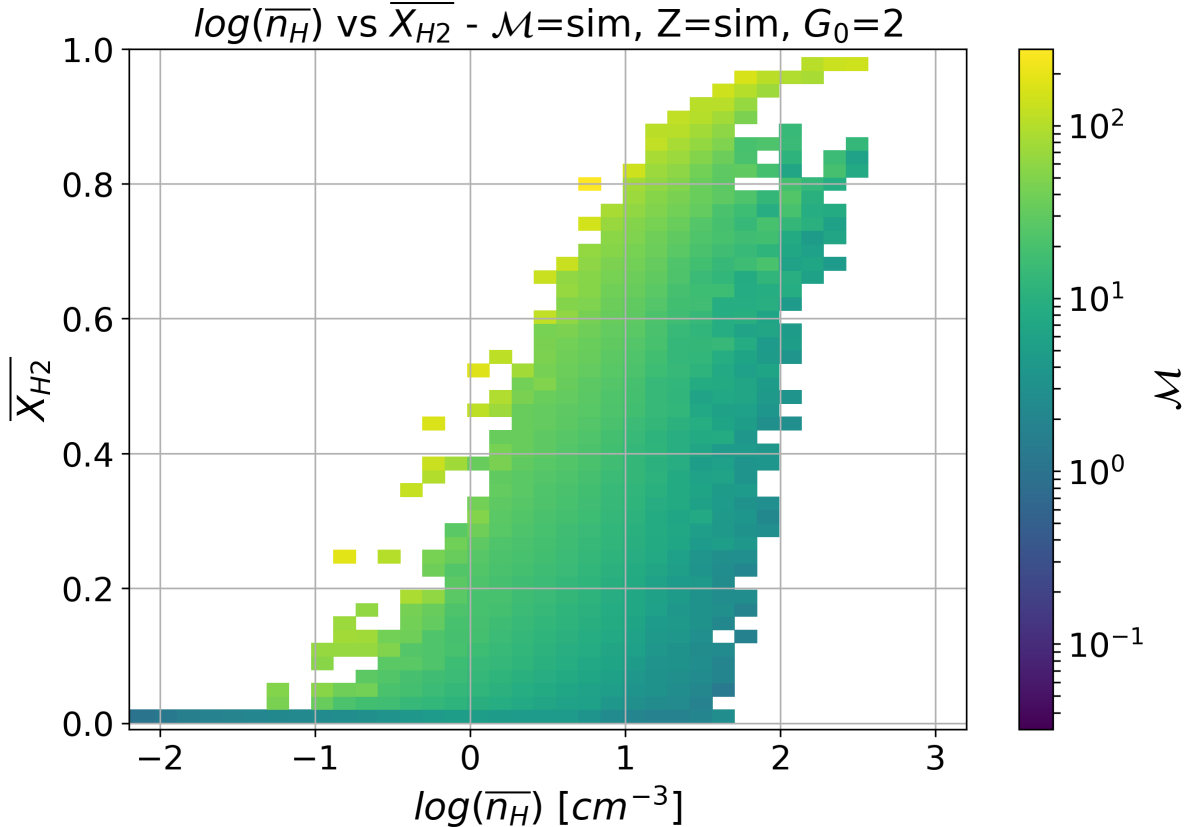


Figure 15: $\overline{X_{H_2}}$ vs $\overline{n_H}$: Plotting the variation of \mathcal{M} - Applying sub-grid model on the simulation.

Figure 15 depicts the distribution of the molecular fraction of H_2 against the mean cell density of the simulation cell. The colour scheme represents the variation of Mach number across the galaxy. As expected, at higher Mach number, more H_2 formation takes place than at a lower Mach number for a given mean cell density. A similar pattern is reproduced for CO in figure 16, where more CO formation takes place at higher Mach number for a given mean cell density.

Figure 17 depicts the distribution of the molecular fraction of H_2 against the mean cell density of the simulation cell. The colour scheme represents the

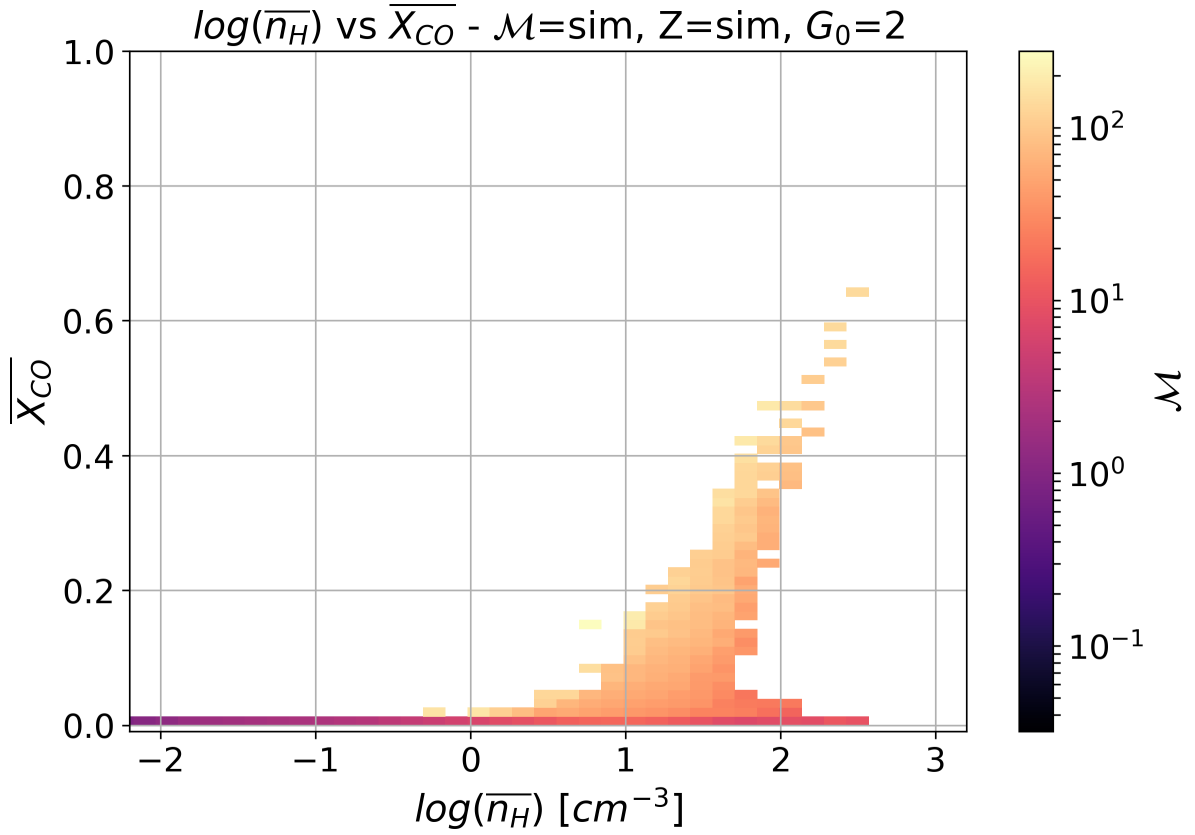


Figure 16: $\overline{X_{CO}}$ vs $\overline{n_H}$: Plotting the variation of \mathcal{M} - Applying sub-grid model on the simulation.

variation of metallicity across the galaxy. As expected, at higher metallicity, more H_2 formation takes place than at a lower metallicity for a given mean cell density. A similar pattern is reproduced for CO in figure 18, where more CO formation takes place at higher metallicity for a given mean cell density.

Figure 19 depicts the mean $\overline{\alpha_{CO}^{-1}}$ factor of $CO(1 - 0)$ transition from each cell in the simulation against the mean cell density of the simulation cell. The turbulent velocity dispersion Δv of each simulation cell is depicted in red, while the isothermal sound speed $c_{s,CO}$ is depicted in blue. Clearly, using the turbulent velocity dispersion is a better option because it produces results closer to the observations from galaxies. The isothermal sound speed $c_{s,CO}$ is not enough for accounting all the motions of volume elements in the simulation cell, which means that the photon emitted from a line transition has a lower escape probability. This results in a lower $\overline{\alpha_{CO}^{-1}}$ as seen from figure 19.

Figure 20 shows the galaxy map of H_2 molecular fractions $\overline{X_{H_2}}$ (weighted

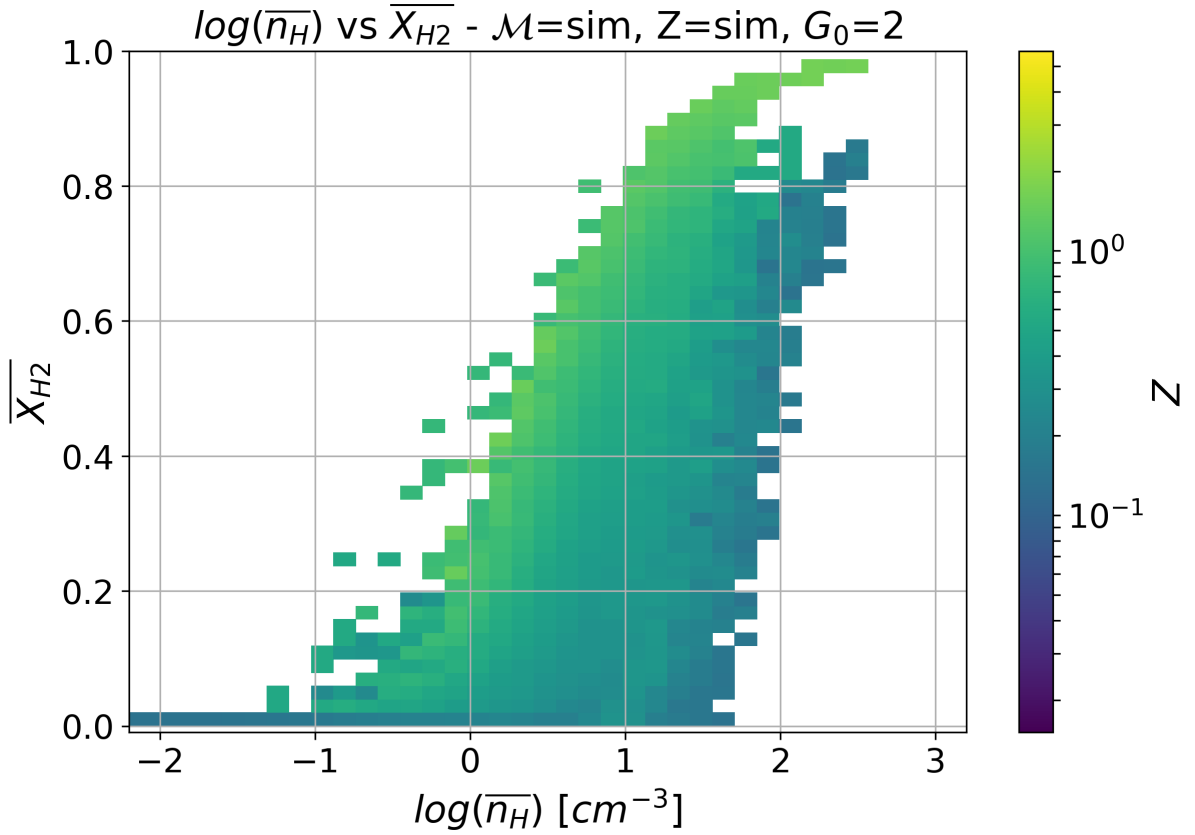


Figure 17: $\overline{X_{H_2}}$ vs $\overline{n_H}$: Plotting the variation of Z - Applying sub-grid model on the simulation.

against mean simulation cell density $\overline{n_H}$) in the galaxy. Figure 21 shows the galaxy map of CO molecular fractions $\overline{X_{CO}}$ (weighted against mean simulation cell density $\overline{n_H}$) in the galaxy. Note the different scales in the colour maps for H_2 and CO . Figure 22 shows the galaxy map of α_{CO}^{-1} factor for line emission of CO (weighted against mean simulation cell density $\overline{n_H}$) in the galaxy.

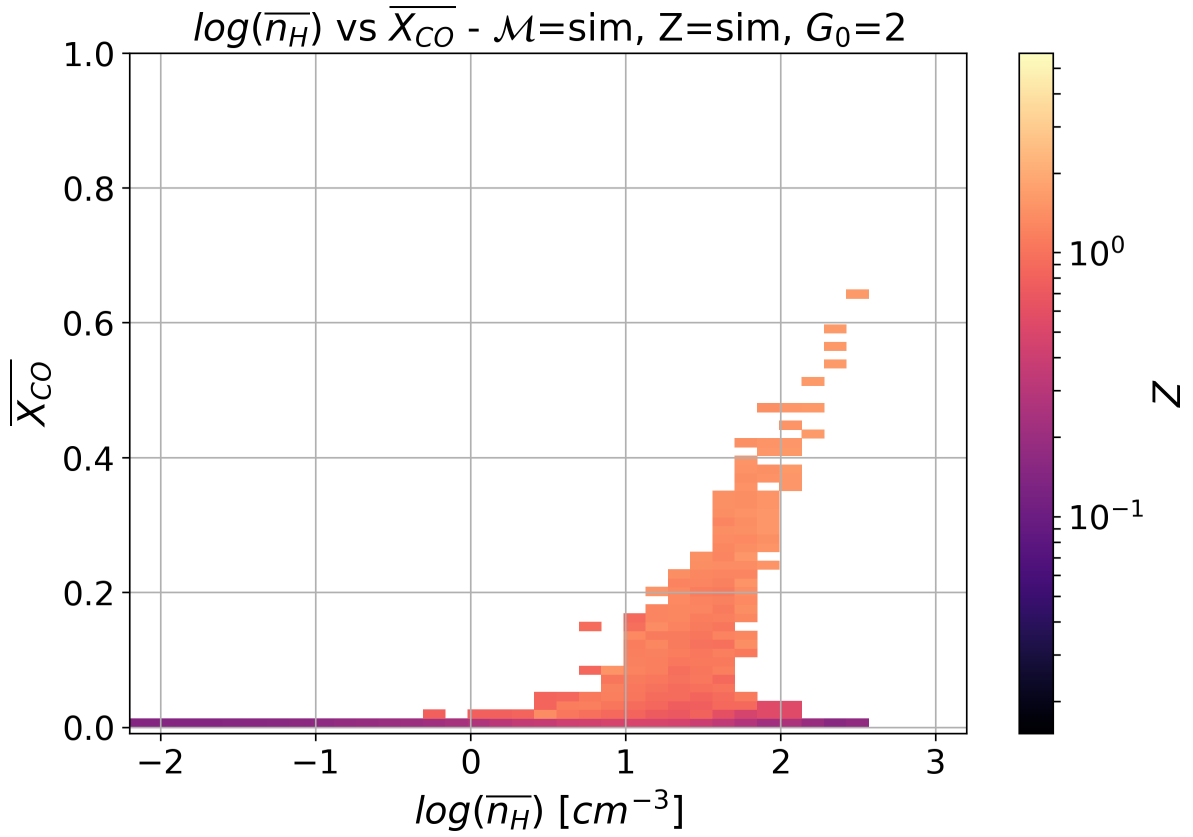


Figure 18: $\overline{X_{CO}}$ vs $\overline{n_H}$: Plotting the variation of Z - Applying sub-grid model on the simulation.

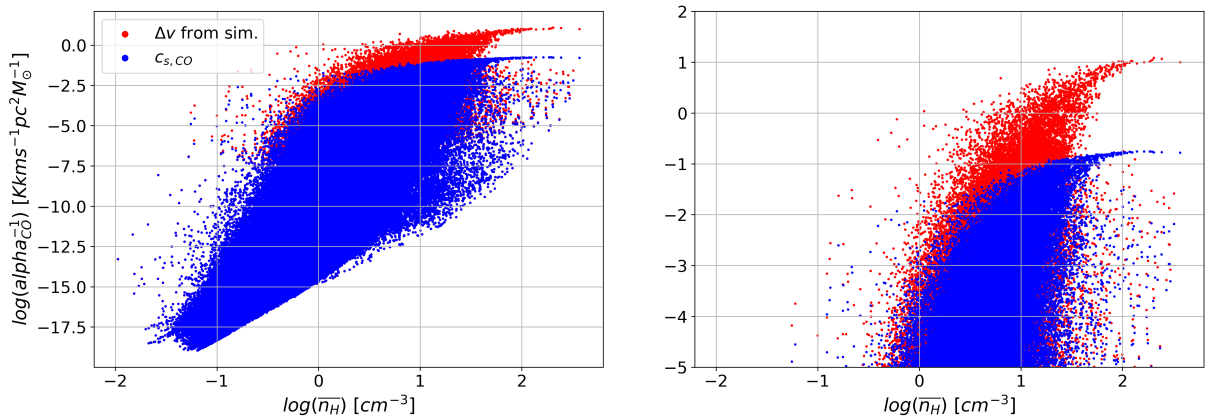


Figure 19: $\log(\overline{\alpha_{CO}^{-1}})$ vs $\log(\overline{n_H})$: Using the Δv and $c_{s,CO}$ values from the simulation - Applying sub-grid model on the simulation.

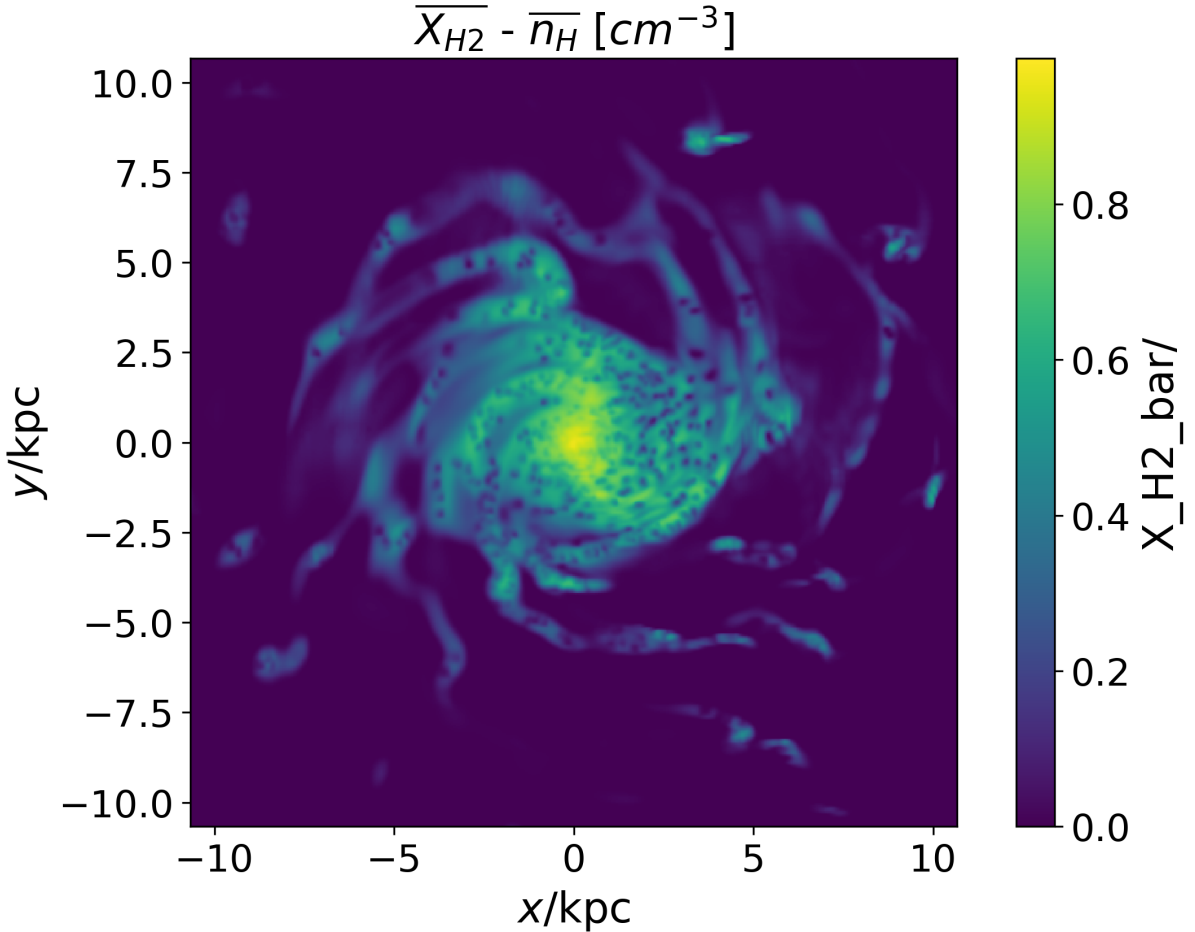


Figure 20: $\overline{X_{H_2}}$ vs $\overline{n_H}$: Galaxy map of the molecular fraction of H_2 - Applying sub-grid model on the simulation.

5 Conclusion

A sub-grid model was constructed that used the mean gas density $\overline{n_H}$, Mach number \mathcal{M} , metallicity Z , and FUV flux G_0 as input parameters and computed the CO line emission of a macroscopic volume element.

The model was then applied on a cosmological zoom-in simulation at $z \approx 0.6$ galaxy ($M_\star \approx 10^{10} M_\odot$, $SFR \approx 2 M_\odot \text{yr}^{-1}$). The assumption was made that all the gas in the simulation is subjected to the same amount of background FUV flux in units of G_0 , which is equal to the SFR of the galaxy simulation in units of $M_\odot \text{yr}^{-1}$.

The results are encapsulated as follows:

- (1) Self-shielding effect of H_2 is a crucial factor in computing molecular abundances of H_2 and CO .

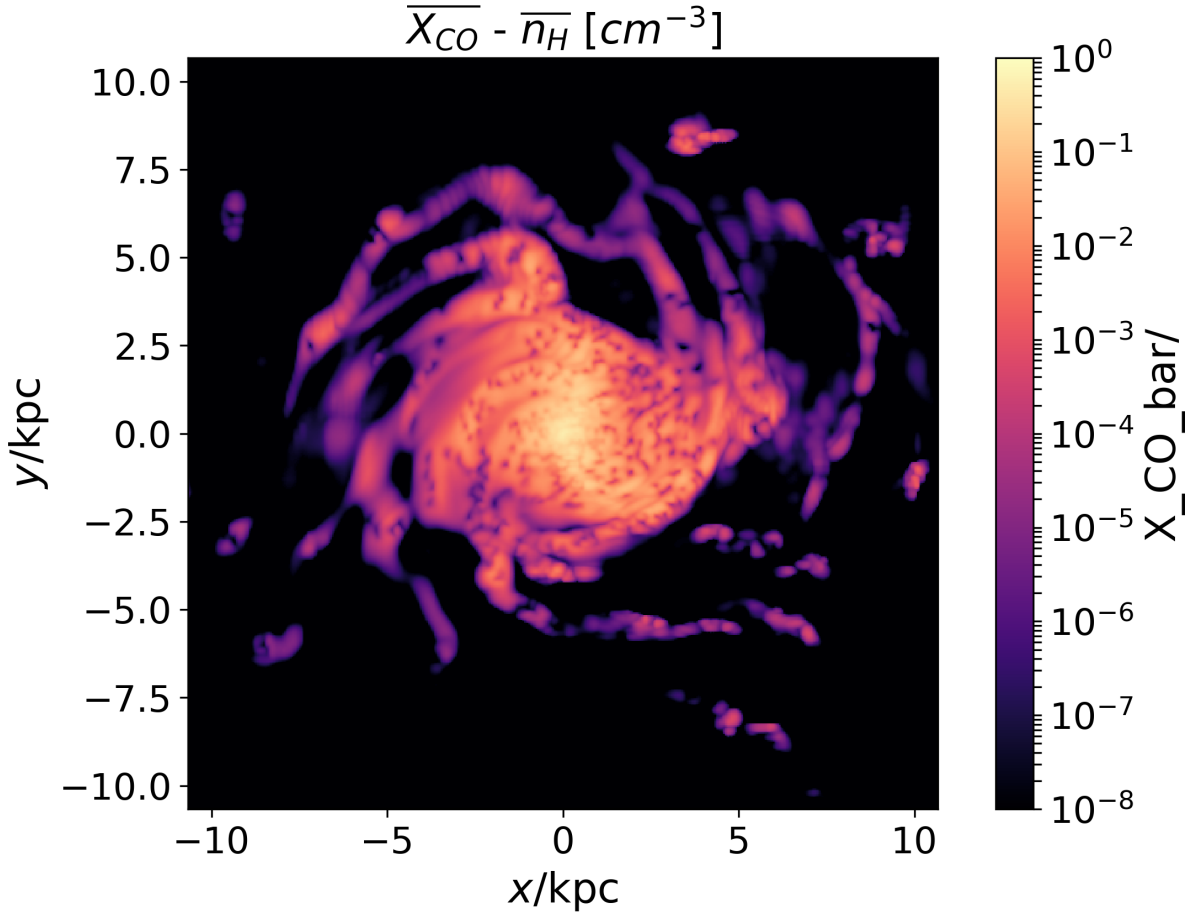


Figure 21: $\overline{X_{CO}}$ vs $\overline{n_H}$: Galaxy map of the molecular fraction of CO - Applying sub-grid model on the simulation.

- (2) H_2 and CO formation is significantly more in cells with large Mach number (\mathcal{M}) and metallicity (Z).
- (3) In typical galaxies, astronomers expect the values of the total mass of H_2 and total luminosity of CO to be $M_{H_2} \approx 2 \times 10^9 M_\odot$ and $L_{CO} \approx 2.5 \times 10^8 \text{Kkms}^{-1}\text{pc}^2$ respectively. The typical value of the factor is $\alpha_{CO}^{-1} \approx 0.25 \text{Kkms}^{-1}\text{pc}^2 M_\odot^{-1}$ While computing the luminosity of the $CO(1 - 0)$ emission line, considering Doppler line broadening due to micro-turbulence produced a result that was closer to the observations from galaxies, than considering Doppler line broadening due to thermal motion of the molecules.
- (4) The total luminosity of the galaxy computed for $CO(1 - 0)$ transition using velocity dispersion Δv is $L_{CO} = 19.48 \times 10^8 \text{Kkms}^{-1}\text{pc}^2$, while total luminosity of the galaxy using isothermal sound speed $c_{s,CO}$ is $L_{CO} = 0.73 \times 10^8 \text{Kkms}^{-1}\text{pc}^2$. The total mass of H_2 in the galaxy is computed to be $M_{H_2} = 2.863 \times 10^9 M_\odot$.

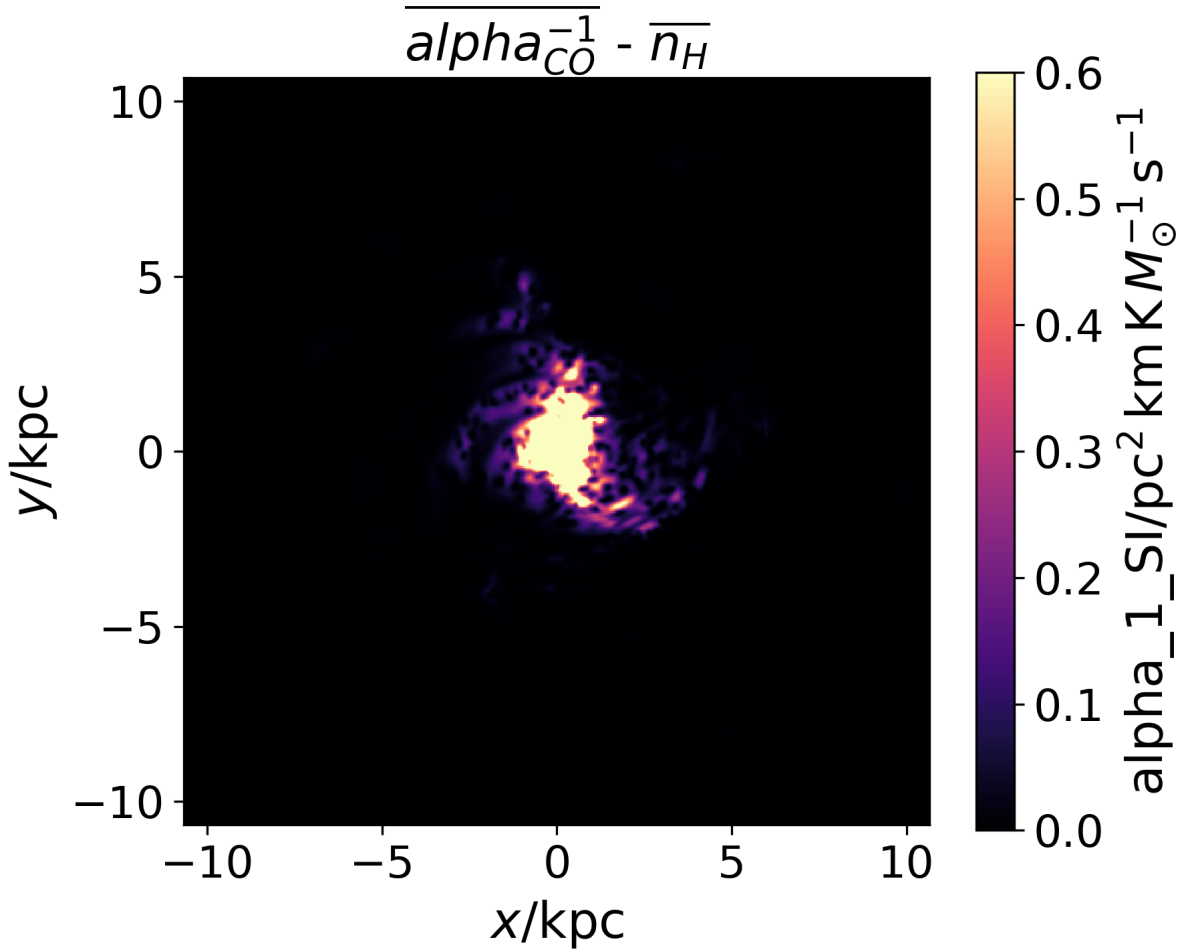


Figure 22: $\overline{\alpha_{CO}^{-1}}$ vs $\overline{n_H}$: Galaxy map of the $\overline{\alpha_{CO}^{-1}}$ factor for line emission of CO - Applying sub-grid model on the simulation.

- (5) Using velocity dispersion Δv , $\alpha_{CO,TOT}^{-1} = 0.684 \text{Kkm s}^{-1} \text{pc}^2 \text{M}_\odot^{-1}$, while using isothermal sound speed c_s, CO , $\alpha_{CO,TOT}^{-1} = 0.0258 \text{Kkm s}^{-1} \text{pc}^2 \text{M}_\odot^{-1}$.
- (6) Contrary to the conclusions of Vallini et al. [7], the role of self-gravity didn't affect the final total luminosity value by much. Also, the difference in LTE vs non-LTE regimes is found to small for CO . The main criteria that affected the total luminosity was the micro-turbulence in each cell. That is why any realistic model for CO formation should provide, together with the other parameters, a model for the micro-turbulence. And only then the other parameters can be predicted accurately.
- (7) The assumption that all the gas in the simulation is subjected to the same amount of background FUV flux, which is equal to the SFR of the galaxy, is a valid assumption because the results obtained are accurate enough.

6 Further Work

(1) In this model, the assumption was made that all the gas in the simulation is subjected to the same amount of background FUV flux in units of G_0 , which is equal to the SFR of the galaxy simulation in units of $M_\odot \text{yr}^{-1}$. A better description for the ISRF profile of the galaxy can be included in future models. This would require the inclusion of full-scale radiative transfer models, that were beyond the scope of this project.

(2) Currently, the temperature used to compute the Jeans length and the population densities is assumed to be equal to the mean temperature, i.e., 10K. This assumption is valid for higher densities, because at lower densities (a few $[H]\text{cm}^3$) the temperature is expected to be higher than 10K, and it will depend on the value of the ISRF. But here in the sub-grid model, clearly, the densities of H_2 and CO are larger than $10^2[H]\text{cm}^3$, that is why this model is probably accurate enough. But if the emissivity of C^+ line emission has to be computed, a sub-grid model for the temperature values will have to be included. This is because CO forms at high densities, so C^+ has to exist at lower densities and disappear at higher densities. And at lower densities the temperature variation will play a bigger role, so the correct value of the temperature is needed.

(3) The self-shielding formula can be modified to include the effects of micro-turbulence of the simulation cell at the scale of Jeans length.

(4) Other lines, such as CN , C^+ , HCO , etc., can also be included in the future iterations of the project. Higher line transitions can also be computed. For higher line transitions, non-LTE might play a more important role.

References

- [1] D. A. Williams W. W. Duley. *Interstellar Chemistry*. Academic Press, 1984.
- [2] Nickolay Y. Gnedin and Bruce T. Draine. Line Overlap and Self-Shielding of Molecular Hydrogen in Galaxies. , 795(1):37, Nov 2014.
- [3] B. T. Draine and Frank Bertoldi. Structure of Stationary Photodissociation Fronts. , 468:269, Sep 1996.
- [4] T. P. Stecher and D. A. Williams. Photodestruction of Hydrogen Molecules in H I Regions. , 149:L29, Jul 1967.
- [5] F. L. Schöier, F. F. S. van der Tak, E. F. van Dishoeck, and J. H. Black. An atomic and molecular database for analysis of submillimetre line observations. , 432(1):369–379, Mar 2005.
- [6] Andrew Fraknoi. *Astronomy*. OpenStax College, Rice University, Open Textbook Library, Houston, Texas Minneapolis, 2016.
- [7] L. Vallini, A. Pallottini, A. Ferrara, S. Gallerani, E. Sobacchi, and C. Behrens. CO line emission from galaxies in the Epoch of Reionization. *Monthly Notices of the Royal Astronomical Society*, 473(1):271–285, 09 2017.
- [8] "C.P. Dullemond". "radiative transfer in astrophysics-lecture notes". "http://www.ita.uni-heidelberg.de/~dullemond/lectures/radtrans_2013/index.shtml?lang=en".
- [9] Woong-Tae Kim, Eve C. Ostriker, and James M. Stone. Magnetorotationally Driven Galactic Turbulence and the Formation of Giant Molecular Clouds. , 599(2):1157–1172, Dec 2003.
- [10] Enrique Vazquez-Semadeni. Hierarchical Structure in Nearly Pressureless Flows as a Consequence of Self-similar Statistics. , 423:681, Mar 1994.
- [11] R. B. Larson. Turbulence and star formation in molecular clouds. , 194:809–826, Mar 1981.

- [12] Chalence Safranek-Shrader, Mark R. Krumholz, Chang-Goo Kim, Eve C. Ostriker, Richard I. Klein, Shule Li, Christopher F. McKee, and James M. Stone. Chemistry and radiative shielding in star-forming galactic discs. *Monthly Notices of the Royal Astronomical Society*, 465(1):885–905, 10 2016.
- [13] Philipp Girichidis, Lukas Konstandin, Anthony P. Whitworth, and Ralf S. Klessen. On the Evolution of the Density Probability Density Function in Strongly Self-gravitating Systems. , 781(2):91, Feb 2014.
- [14] Daniel J. Price and Christoph Federrath. A comparison between grid and particle methods on the statistics of driven, supersonic, isothermal turbulence. , 406(3):1659–1674, Aug 2010.
- [15] Christoph Federrath and Ralf S. Klessen. ON THE STAR FORMATION EFFICIENCY OF TURBULENT MAGNETIZED CLOUDS. *The Astrophysical Journal*, 763(1):51, jan 2013.
- [16] Ralf S. Klessen. The formation of stellar clusters: Time-varying protostellar accretion rates. *The Astrophysical Journal*, 550(1):L77–L80, mar 2001.
- [17] David C. Collins, Alexei G. Krutsuk, Paolo Padoan, Hui Li, Hao Xu, Sergey D. Ustyugov, and Michael L. Norman. THE TWO STATES OF STAR-FORMING CLOUDS. *The Astrophysical Journal*, 750(1):13, apr 2012.
- [18] J. Kainulainen, H. Beuther, T. Henning, and R. Plume. Probing the evolution of molecular cloud structure. From quiescence to birth. , 508(3):L35–L38, Dec 2009.
- [19] N. Schneider, T. Csengeri, M. Hennemann, F. Motte, P. Didelon, C. Federrath, S. Bontemps, J. Di Francesco, D. Arzoumanian, and V. Minier. Cluster-formation in the Rosette molecular cloud at the junctions of filaments. , 540:L11, Apr 2012.
- [20] Franck Le Petit, Cyrine Nehmé, Jacques Le Bourlot, and Evelyne Roueff. A Model for Atomic and Molecular Interstellar Gas: The Meudon PDR Code. , 164(2):506–529, Jun 2006.

- [21] Simon C. O. Glover and Paul C. Clark. Approximations for modelling CO chemistry in giant molecular clouds: a comparison of approaches. , 421(1):116–131, Mar 2012.
- [22] Michael Kretschmer and Romain Teyssier. Forming early-type galaxies without AGN feedback: a combination of merger-driven outflows and inefficient star formation. *arXiv e-prints*, page arXiv:1906.11836, Jun 2019.
- [23] R. Teyssier. Cosmological hydrodynamics with adaptive mesh refinement. A new high resolution code called RAMSES. , 385:337–364, Apr 2002.